



Calculation of predictions for non-identical particle correlations in heavy ions collisions at LHC energies from hydrodynamics-inspired models

MASTER OF SCIENCE THESIS

Author:
Mateusz Wojciech Gałażyn

Supervisor:
Prof. Adam Kisiel

Warsaw, 1st December 2014



Wyznaczenie przewidywań teoretycznych dla korelacji cząstek nieidentycznych w zderzeniach ciężkich jonów przy energiach LHC w modelach opartych na hydrodynamice

PRACA MAGISTERSKA

Autor:
Mateusz Wojciech Gałażyn

Promotor:
dr hab. inż. Adam Kisiel, prof. PW

Warszawa, 1 grudnia 2014

1 Abstract

2 This thesis presents results of two-particle momentum correlations analysis
3 for different kinds of particles produced in heavy ion collisions. The studies
4 were carried for the data from lead-lead collisions at the centre of mass
5 energy $\sqrt{s_{NN}} = 2.76$ TeV simulated in the THERMINATOR model using the
6 (3+1)-dimensional hydrodynamic model with viscosity. Analysis was performed
7 for the three particle kinds: pions, kaons and protons for the collisions in eight
8 different centrality ranges.

9 The THERMINATOR model allows to perform statistical hadronization of
10 stable particles and unstable resonances from a given hypersurface which is
11 followed by the resonance propagation and decay phase. The four-dimensional
12 hypersurface is coming from the calculations performed on a basis of relativistic
13 hydrodynamic framework with the viscosity corrections.

14 One can investigate space-time characteristics of the particle-emitting source
15 through two-particle interferometry using experimental observables. The
16 experimental-like analysis of the data coming from a model calculations yields
17 a possibility to test the hydrodynamic description of a quark-gluon plasma.
18 This thesis concentrates on the verification of the prediction of appearance of
19 femtoscopic radii scaling with the transverse mass.

20 The three dimensional correlation functions were calculated using spherical
21 harmonics decomposition. One can use this approach to perform calculations
22 with lower statistics and moreover the visualization of results is much easier. The
23 calculated correlation functions show expected increase of a correlation for pions
24 and kaons at the low relative momenta of a pair. For the protons at the same mo-
25 mentum region, the decrease occurs. The transverse pair momentum and cen-
26 trality dependence on a correlation function is observed. In order to perform the
27 quantitative analysis of this influence, the fitting of theoretical formula for cor-
28 relation function was performed. The femtoscopic radii calculated in the LCMS
29 and PRF are falling with the transverse mass m_T . To test the scaling predicted
30 from the hydrodynamics, the power law was fitted $\alpha m_T^{-\beta}$. The radii calculated
31 for pions, kaons and protons in the LCMS are following the common scaling. In
32 case of the PRF no such scaling is observed. To recover the scaling in the PRF, the
33 approximate factor is proposed: $\sqrt{(\sqrt{\gamma_T} + 2)/3}$. The radii in the PRF divided by
34 the proposed scaling factor are falling on the common curve, therefore the scaling
35 can be recovered using the proposed scaling factor. The experimental analysis is
36 usually performed in the PRF (requires less statistics), hence the method of scal-
37 ing recovery enables easier testing of the hydrodynamic predictions, which are
38 not visible in the PRF.

Streszczenie

40 W tej pracy zaprezentowane są wyniki analizy dwucząstkowych korelacji pę-
 41 dowych dla trzech różnych typów cząstek produkowanych w zderzeniach cięż-
 42 kich jonów. Obliczenia zostały wykonane dla danych ze zderzeń ołów-ołów przy
 43 energii w centrum masy $\sqrt{s_{NN}} = 2.76$ TeV wygenerowanych za pomocą mo-
 44 delu THERMINATOR przy użyciu (3+1)-wymiarowego modelu hydrodynamicz-
 45 nego uwzględniającego lepkość ośrodka. Analiza została wykonana dla trzech
 46 rodzajów cząstek: pionów, kaonów i protonów dla dziewięciu różnych przedzia-
 47 łów centralności.

48 Model THERMINATOR pozwala na wykonanie statystycznej hadronizacji
 49 stabilnych cząstek jak i również niestabilnych rezonansów z danej
 50 hiperpowierzchni wymrażania, a następnie uwzględnienie propagacji i
 51 rozpadów tych rezonansów. Czterowymiarowa hiperpowierzchnia pochodzi z
 52 obliczeń przeprowadzonych na podstawie hydrodynamiki relatywistycznej z
 53 uwzględnieniem poprawek pochodzących od lepkości.

54 Interferometria dwucząstkowa pozwala na zbadanie charakterystyk
 55 czasowo-przestrzennych źródła cząstek. Poprzez analizę danych pochodzących
 56 z obliczeń modelowych można dokonać sprawdzenia zakresu stosownalności
 57 hydrodynamiki do opisu właściwości plazmy kwarkowo-gluonowej. Ta praca
 58 koncentruje się na weryfikacji skalowania promieni femtoskopowych z masą
 59 poprzeczną przewidywanego przez hydrodynamikę.

60 Trójwymiarowe funkcje korelacyjne zostały obliczone za pomocą rozkładu w
 61 szeregu harmonik sferycznych. To podejście wymaga mniejszej statystyki i po-
 62zwala na łatwiejszą wizualizację wyników. Obliczone funkcje korelacyjne wy-
 63kazują oczekiwany wzrost korelacji dla niskich różnic pędów dla par pionów i
 64 kaonów. Dla par protonów w tym samym zakresie pędów widoczny jest spa-
 65dek korelacji. Widoczny jest wpływ pędu poprzecznego pary oraz centralności
 66 na funkcję korelacyjną. W celu wykonania analizy ilościowej tego wpływu, zo-
 67stało wykonane dopasowanie formuły analitycznej do obliczonych funkcji kore-
 68 lacyjnych. Otrzymane w ten sposób promienie femtoskopowe w LCMS i PRF
 69 wykazują spadek wraz z wzrostem masy poprzecznej m_T . W celu sprawdzenie
 70 skalowania przewidywanego przez hydrodynamikę została dopasowana zależ-
 71 ność potęgowa: $\alpha m_T^{-\beta}$. Promienie obliczone dla pionów, kaonów i protonów
 72 zachowują wzajemne skalowanie w LCMS. W przypadku PRF skalowanie nie
 73 jest widoczne. Aby odzyskać skalowanie w PRF, został zaproponowany przy-
 74 bliżony współczynnik: $\sqrt{(\sqrt{\gamma_T} + 2)/3}$. Promienie w PRF po podzieleniu przez

⁷⁵ współczynnik skalowania, są opisywalne przez podaną zależność potęgową, za-
⁷⁶ tem umożliwia on odzyskanie skalowania. Analiza eksperimentalna jest zazwy-
⁷⁷ czaj wykonywana w PRF (wymaga mniejszej statystyki), zatem ta metoda po-
⁷⁸ zwala na łatwiejszą weryfikację przewidywań hydrodynamiki które są widoczne
⁷⁹ w LCMS, a nie są w PRF.

⁸⁰ Contents

⁸¹	Introduction	1
⁸²	1 Theory of heavy ion collisions	3
⁸³	1.1 The Standard Model	3
⁸⁴	1.2 Quantum Chromodynamics	4
⁸⁵	1.2.1 Quarks and gluons	4
⁸⁶	1.2.2 Quantum Chromodynamics potential	5
⁸⁷	1.2.3 The quark-gluon plasma	7
⁸⁸	1.3 Relativistic heavy ion collisions	9
⁸⁹	1.3.1 Stages of heavy ion collision	9
⁹⁰	1.3.2 QGP signatures	11
⁹¹	2 Therminator model	19
⁹²	2.1 (3+1)-dimensional viscous hydrodynamics	19
⁹³	2.2 Statistical hadronization	20
⁹⁴	2.2.1 Cooper-Frye formalism	21
⁹⁵	2.3 Events generation procedure	22
⁹⁶	3 Particle interferometry	25
⁹⁷	3.1 HBT interferometry	25
⁹⁸	3.2 Theoretical approach	25
⁹⁹	3.2.1 Conventions used	26
¹⁰⁰	3.2.2 Two particle wave function	27
¹⁰¹	3.2.3 Source emission function	28
¹⁰²	3.2.4 Analytical form of a correlation function	30
¹⁰³	3.2.5 Spherical harmonics decomposition of a correlation function	31
¹⁰⁴	3.3 Experimental approach	32
¹⁰⁵	3.4 Scaling of femtoscopic radii	33
¹⁰⁶	3.4.1 Scaling in LCMS	34
¹⁰⁷	3.4.2 Scaling in PRF	35
¹⁰⁸	4 Results	36
¹⁰⁹	4.1 Identical particles correlations	36
¹¹⁰	4.1.1 Spherical harmonics components	36

111	4.1.2	Centrality dependence of a correlation function	40
112	4.1.3	k_T dependence of a correlation function	41
113	4.2	Results of the fitting procedure	42
114	4.2.1	The three-dimensional femtoscopic radii scaling	42
115	4.2.2	Scaling of one-dimensional radii	46
116	4.3	Discussion of the results	47
117	Conclusions		48
118	A	Scripts for correlation function calculations	50
119	A.1	Events generation	50
120	A.2	Calculations of experimental-like correlation functions	51
121	B	Macros for fitting	52
122	C	Plotting scripts	53

¹²³ Introduction

Many people were trying to discover what was in the beginning of the Universe which we observe today. Through the years, more or less successful theories were appearing and trying to describe its origin and behaviour. Among them is one model, which provides a comprehensive explanation for a broad range of phenomena, including the cosmic microwave background, abundance of the light elements and Hubble's law. This model is called The Big Bang theory and has been born in 1927 on the basis of principles proposed by the Belgian priest and scientist Georges Lemaître. Using this model and known laws of physics one can calculate the characteristics of the Universe in detail back in time to the extreme densities and temperatures. However, at some point these calculations fail. The extrapolation of the expansion of the Universe backwards in time using general relativity yields an infinite density and temperature at a finite time in the past. This appearance of singularity is a signal of the breakdown of general relativity. The range of this extrapolation towards singularity is debated - certainly we can go no closer than the end of *Planck epoch* i.e. 10^{-43} s. At this very first era the temperature of the Universe was so high, that the four fundamental forces - electromagnetism, gravitation, weak nuclear interaction and strong nuclear interaction - were one fundamental force. Between 10^{-43} s and 10^{-36} s of a lifetime of the Universe, there is a *grand unification epoch*, at which forces are starting to separate from each other. The *electroweak epoch* lasted from 10^{-36} s to 10^{-12} s, when the strong force separated from the electroweak force. After the electroweak epoch, there was the *quark epoch* in which the Universe was a dense "soup" of quarks. During this stage the fundamental forces of gravitation, electromagnetism, strong and weak interactions had taken their present forms. The temperature at this moment was still too high to allow quarks to bind together and form hadrons. At the end of quark era, there was a big freeze-out - when the average energy of particle interactions had fallen below the binding energy of hadrons. This era, in which quarks became confined into hadrons, is known as the *hadron epoch*. At this moment the matter had started forming nuclei and atoms, which we observe today.

Here arises the question: how can we study the very beginning of the Universe? To do this, one should create in a laboratory a system with such a large density and high temperature to recreate those conditions. Today, this is achievable through sophisticated machines, which are particle accelerators. In

158 the particle accelerators, like the Large Hadron Collider at CERN, Geneva or
159 Relativistic Heavy Ion Collider at Brookhaven National Laboratory in Upton,
160 New York, the heavy ions after being accelerated to near the speed of light are
161 collided in order to generate extremely dense and hot phase of matter and
162 recreate the quark-gluon plasma. The plasma is believed to behave like an
163 almost ideal fluid and to become a medium, that can be described by the laws of
164 relativistic hydrodynamics.

165 This thesis is providing predictions for collective behaviour of the quark-
166 gluon plasma coming from the hydrodynamic equations. Experimental-like
167 analysis was performed for the high energy Pb-Pb collisions generated with
168 THERMINATOR model.

169 The 1st chapter is an introduction to the theory of heavy ion collisions. It
170 contains the brief description of the Standard Model and Quantum Chromody-
171 namics. The quark-gluon plasma and its signatures are also characterized.

172 In the 2nd chapter, the relativistic hydrodynamic framework and the
173 THERMINATOR model used to perform the simulations of collisions are
174 characterized.

175 The 3rd chapter covers the particle interferometry method used in this
176 work. The effects coming from the hydrodynamics in the experimental results
177 for particle interferometry are also presented. An algorithm of building
178 experimental correlation functions is also described in this chapter.

179 In the 4th chapter, a detailed analysis of the results for two-particle femto-
180 scopy for different pairs of particles is presented. The quantitative analysis of
181 calculated femtoscopic radii as well as the appearance of transverse mass scaling
182 is discussed.

¹⁸³ **Chapter 1**

¹⁸⁴ **Theory of heavy ion collisions**

¹⁸⁵ **1.1 The Standard Model**

¹⁸⁶ In the 1970s, a new theory of fundamental particles and their interaction
¹⁸⁷ emerged. It was a new concept, which combines the electromagnetic, weak and
¹⁸⁸ strong nuclear interactions between known particles. This theory is called *The*
¹⁸⁹ *Standard Model*. There are seventeen named particles in the standard model, or-
¹⁹⁰ ganized into the chart shown below (Fig. 1.1). Fundamental particles are divided
into two families: *fermions* and *bosons*.

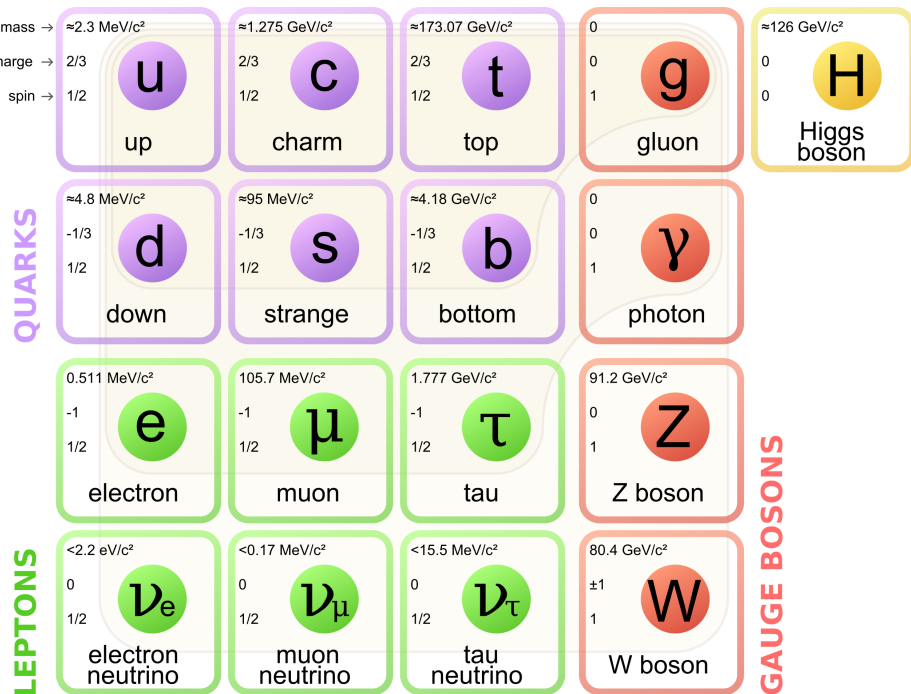


Figure 1.1: The Standard Model of elementary particles [1].

191 Fermions are the building blocks of matter. They are divided into two groups.
 192 Six of them, which must bind together are called *quarks*. Quarks are known to
 193 bind into doublets (*mesons*), triplets (*baryons*) and recently confirmed four-quark
 194 states.¹ Two of baryons, with the longest lifetimes, are forming a nucleus: a pro-
 195 ton and a neutron. A proton is build from two up quarks and one down, and
 196 neutron consists of two down quarks and one up. A proton is found to be a stable
 197 particle (at least it has a lifetime larger than 10^{35} years) and a free neutron has a
 198 mean lifetime about 8.8×10^2 s. Fermions, that can exist independently are called
 199 *leptons*. Neutrinos are a subgroup of leptons, which are only influenced by weak
 200 interaction. Fermions can be divided into three generations (three columns in
 201 the Figure 1.1). Generation I particles can combine into hadrons with the longest
 202 life spans. Generation II and III consists of unstable particles which also form
 203 unstable hadrons.

204 Bosons are force carriers. There are four fundamental forces: weak - respons-
 205 ible for radioactive decay, strong - coupling quarks into hadrons, electromagnetic
 206 - between charged particles and gravity - the weakest, which causes the attraction
 207 between particles with mass. The Standard Model describes the first three. The
 208 weak force is mediated by W^\pm and Z^0 bosons, electromagnetic force is carried by
 209 photons γ and the carriers of a strong interaction are gluons g . The fifth boson is
 210 a Higgs boson which is responsible for giving other particles mass.

211 1.2 Quantum Chromodynamics

212 1.2.1 Quarks and gluons

213 Quarks interact with each other through the strong interaction. The medi-
 214 ator of this force is a *gluon* - a massless and electrical chargeless particle. In the
 215 quantum chromodynamics (QCD) - theory describing strong interaction - there
 216 are six types of "charges" (like electrical charges in the electrodynamics) called
 217 *colours*. The colours were introduced because some of the observed particles, like
 218 Δ^- , Δ^{++} and Ω^- appeared to consist of three quarks with the same flavour (*ddd*,
 219 *uuu* and *sss* respectively), which was in conflict with the Pauli principle. One
 220 quark can carry one of the three colours (usually called *red*, *green* and *blue*) and anti-
 221 quark one of the three anti-colours respectively. Only colour-neutral (or white)
 222 particles could exist. Mesons are assumed to be a colour-anticolour pair, while
 223 baryons are *red-green-blue* triplets. Gluons also are colour-charged and there are
 224 8 types of gluons. Therefore they can interact with themselves [3].

¹The LHCb experiment at CERN in Geneva confirmed recently the existence of $Z(4430)$ - a particle consisting of four quarks [2].

225 **1.2.2 Quantum Chromodynamics potential**

226 As a result of the fact that gluons are massless, one can expect, that the static
 227 potential in QCD will have the form like similar one in electrodynamics e.g.
 228 $\sim 1/r$ (by analogy to photons). In reality the QCD potential is assumed to have
 229 the form of [3]

$$V_s = -\frac{4}{3} \frac{\alpha_s}{r} + kr, \quad (1.1)$$

230 where the α_s is a coupling constant of the strong force and the kr part is related
 231 with *confinement*. In comparison to the electromagnetic force, a value of the strong
 232 coupling constant is $\alpha_s \approx 1$ and the electromagnetic one is $\alpha = 1/137$.

233 The fact that quarks does not exist separately and are always bound, is called
 234 confinement. As two quarks are pulled apart, the linear part kr in the Eq. 1.1
 235 becomes dominant and the potential becomes proportional to the distance. This
 236 situation resembles stretching of a string. At some point, when the string is so
 237 large it is energetically favourable to create a quark-antiquark pair. At this
 238 moment such pair (or pairs) is formed, the string breaks and the confinement is
 preserved (Fig. 1.2).

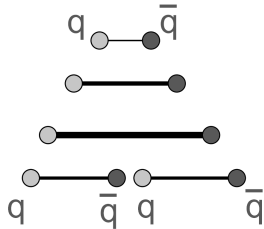


Figure 1.2: A string breaking and a creation of a new quark-antiquark pair [4].

239
 240 On the other hand, for small r , an interaction between the quarks and gluons
 241 is dominated by the Coulomb-like term $-\frac{4}{3} \frac{\alpha_s}{r}$. The coupling constant α_s depends
 242 on the four-momentum Q^2 transferred in the interaction. This dependence is
 243 presented in Fig. 1.3. The value α_s decreases with increasing momentum trans-
 244 fer and the interaction becomes weak for large Q^2 , i.e. $\alpha_s(Q) \rightarrow 0$. Because
 245 of the weakening of coupling constant, quarks at large energies (or small dis-
 246 tances) are starting to behave like free particles. This phenomenon is known as
 247 *asymptotic freedom*. The QCD potential also has temperature dependence - the
 248 force strength "melts" with the temperature increase. Therefore the asymptotic
 249 freedom is expected to appear in either the case of high baryon densities (small
 250 distances between quarks) or very high temperatures. This temperature depend-
 251 ence is illustrated in Fig. 1.4.

252 If the coupling constant α_s is small, one can use perturbative methods to cal-
 253 culate physical observables. Perturbative QCD (pQCD) successfully describes
 254 hard processes (with large Q^2), such as jet production in high energy proton-
 255 antiproton collisions. The applicability of pQCD is defined by the *scale parameter*



Figure 1.3: The coupling parameter α_s dependence on four-momentum transfer Q^2 [5].

256 $\Lambda_{QCD} \approx 200$ MeV. If $Q \gg \Lambda_{QCD}$ then the process is in the perturbative domain
 257 and can be described by pQCD. A description of soft processes (when $Q < 1$ GeV)
 258 is a problem in QCD - perturbative theory breaks down at this scale. Therefore,
 259 to describe processes with low Q^2 , one has to use alternative methods like Lattice
 260 QCD. Lattice QCD (LQCD) is non-perturbative implementation of a field theory
 261 in which QCD quantities are calculated on a discrete space-time grid. LQCD al-
 262 lows to obtain properties of matter in equilibrium, but there are some limitations.
 263 Lattice QCD requires fine lattice spacing to obtain precise results - therefore large
 264 computational resources are necessary. With the constant growth of computing
 265 power this problem will become less important. The second problem is that lat-
 266 tice simulations are possible only for baryon density $\mu_B = 0$. At $\mu_B \neq 0$, Lattice
 267 QCD breaks down because of the sign problem. In QCD the thermodynamic
 268 observables are related to the grand canonical partition function, which has a ba-
 269 ryonic chemical potential μ_B as a parameter. Therefore, the baryonic density can
 270 be controlled by tuning the baryonic chemical potential. For fermions μ_B can be
 271 both positive and negative. For a particles with μ_B , their antiparticles have chem-
 272 ical potentials with opposite sign $-\mu_B$. Since at the early universe the number of
 273 baryons and antibaryons were almost equal we can use $\mu_B = 0$ to a very good
 274 approximation [6].

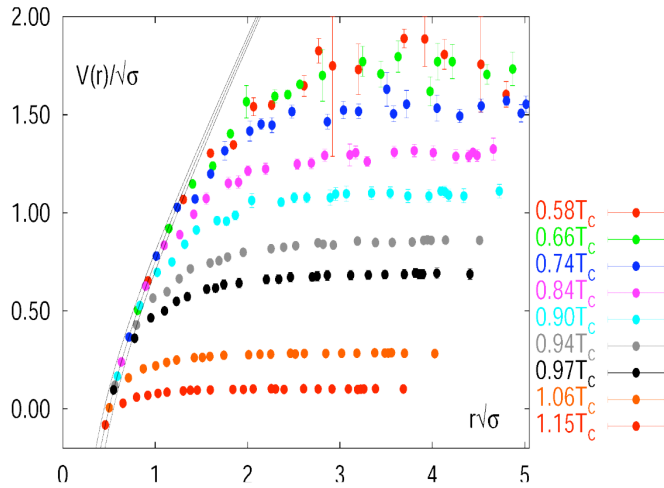


Figure 1.4: The QCD potential for a quark-antiquark pair as a function of distance for different temperatures. A value of a potential decreases with the temperature [4].

1.2.3 The quark-gluon plasma

The new state of matter in which quarks are no longer confined is known as a *quark-gluon plasma* (QGP). The predictions coming from the discrete space-time Lattice QCD calculations reveal a phase transition from the hadronic matter to the quark-gluon plasma at the high temperatures and baryon densities. The results obtained from such calculations are shown on Fig. 1.5. The energy density ϵ which is divided by T^4 is a measure of the number of degrees of freedom in

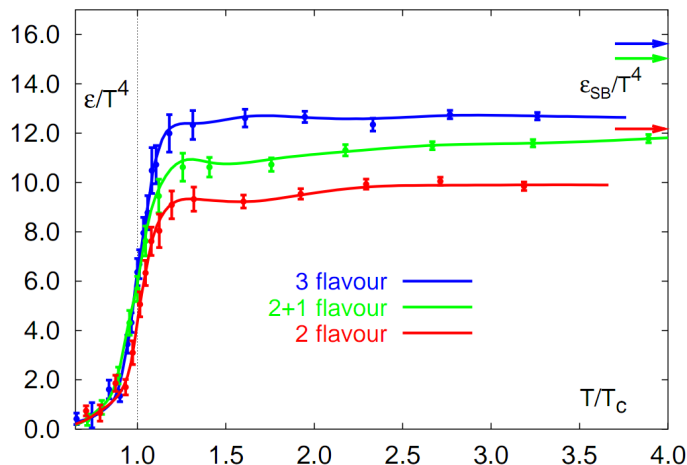


Figure 1.5: A number of degrees of freedom as a function of a temperature [7].

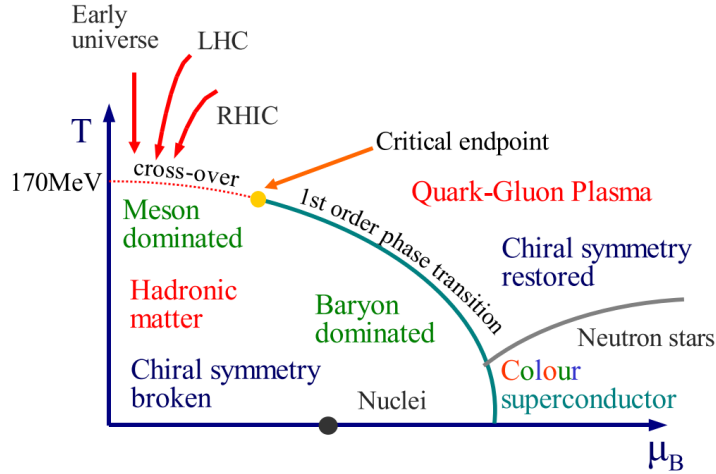


Figure 1.6: Phase diagram coming from the Lattice QCD calculations [8].

282 the system. One can observe significant rise of this value, when the temperature
 283 increases past the critical value T_C . Such increase is signaling a phase transition
 284 - the formation of QGP [8]. The values of the energy densities plotted in Fig. 1.5
 285 do not reach the Stefan-Boltzmann limit ϵ_{SB} (marked with arrows), which corre-
 286 sponds to an ideal gas. This can indicate some residual interactions in the system.
 287 According to the results from the RHIC², the new phase of matter behaves more
 288 like an ideal fluid, than like a gas [9].

289 One of the key questions, to which current heavy ion physics tries to find an
 290 answer is the value of a critical temperature T_C as a function of a baryon chem-
 291 ical potential μ_B (baryon density), where the phase transition occurs. The results
 292 coming from the Lattice QCD are presented in Fig. 1.6. The phase of matter in
 293 which quarks and gluons are deconfined is expected to exist at large temperat-
 294 ures. In the region of small temperatures and high baryon densities, a differ-
 295 ent state is supposed to appear - a *colour superconductor*. The phase transition
 296 between hadronic matter and the QGP is thought to be of 1st order at $\mu_B \gg 0$.
 297 However as $\mu_B \rightarrow 0$ quarks' masses become significant and a sharp transition
 298 transforms into a rapid but smooth cross-over. It is believed that in Pb-Pb colli-
 299 sions observed at the LHC³, the created matter has high enough temperature to
 300 be in the quark-gluon plasma phase, then cools down and converts into hadrons,
 301 undergoing a smooth transition [8].

²Relativistic Heavy Ion Collider at Brookhaven National Laboratory in Upton, New York

³Large Hadron Collider at CERN, Geneva

302 1.3 Relativistic heavy ion collisions

303 1.3.1 Stages of heavy ion collision

304 To create the quark-gluon plasma one has to achieve high enough temper-
 305 atures and baryon densities. Such conditions can be recreated in the heavy ion
 collisions at the high energies. The left side of the Figure 1.7 shows simplified

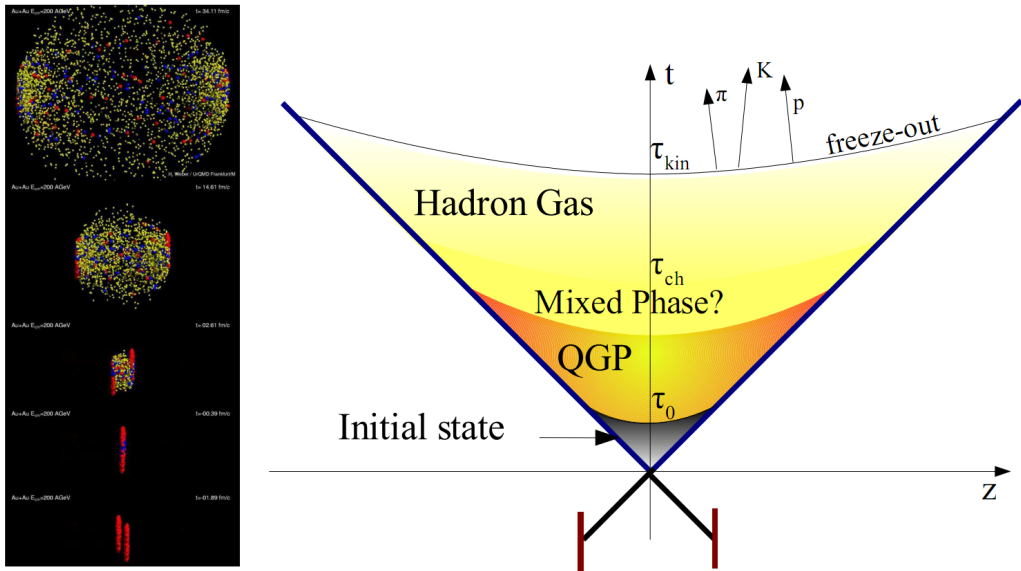


Figure 1.7: Left: stages of a heavy ion collision simulated in the UrQMD model.
 Right: schematic view of a heavy ion collision evolution [8].

306 picture of a central collision of two highly relativistic nuclei in the centre-of-
 307 mass reference frame. The colliding nuclei are presented as thin disks because
 308 of the Lorentz contraction. In the central region, where the energy density is the
 309 highest, a new state of matter - the quark-gluon plasma - is supposedly created.
 310 Afterwards, the plasma expands ad cools down, quarks combine into hadrons
 311 and their mutual interactions cease when the system reaches the *freeze-out* tem-
 312 perature. Subsequently, produced free hadrons move towards the detectors.
 313

314 On the right side of the Figure 1.7 a space-time evolution of a collision process
 315 is presented, plotted in the light-cone variables (z , t). The two highly relativistic
 316 nuclei are traveling basically along the light cone until they collide at the centre
 317 of the diagram. Nuclear fragments emerge from the collision again along the
 318 (forward) light cone, while the matter between fragmentation zones populates
 319 the central region. This hot and dense matter is believed to be in the state of the
 320 quark-gluon plasma. Several frameworks exist to describe this transition to the
 321 QGP phase, for example: QCD string breaking, QCD parton cascades or colour
 322 glass condensate evolving into glasma and later into quark-gluon plasma [10].

323 **String breaking** – In the string picture, the nuclei pass through each other forming colour strings. This is analogous to the situation depicted in the Fig 1.2 - the
 324 colour string is created between quarks inside particular nucleons in nuclei. In
 325 the next step strings decay / fragment forming quarks and gluons or directly
 326 hadrons. This approach becomes invalid at very high energies, when the strings
 327 overlap and cannot be treated as independent objects.

328 **Parton cascade** – The parton⁴ cascade model is based on the pQCD. The colliding
 329 nuclei are treated as clouds of quarks which penetrate through each other.
 330 The key element of this method is the time evolution of the parton phase-space
 331 distributions, which is governed by a relativistic Boltzmann equation with a col-
 332 lision term that contains dominant perturbative QCD interactions. The bottleneck
 333 of the parton cascade model is the low energies regime, where the Q^2 is too small
 334 to be described by the perturbative theory.

335 **Colour glass condensate** – The colour glass condensate assumes, that the had-
 336 ion can be viewed as a tightly packed system of interacting gluons. The sat-
 337 uration of gluons increases with energy, hence the total number of gluons may
 338 increase without bound. Such a saturated and weakly coupled gluon system is
 339 called a colour glass condensate. The fast gluons in the condensate are Lorentz
 340 contracted and redistributed on the two very thin sheets representing two col-
 341 liding nuclei. The sheets are perpendicular to the beam axis. The fast gluons
 342 produce mutually orthogonal colour magnetic and electric fields, that only ex-
 343 ist on the sheets. Immediately after the collision, i.e. just after the passage of
 344 the two gluonic sheets through each other, the longitudinal electric and magnetic
 345 fields are produced forming the *glasma*. The glasma fields decay through the
 346 classical rearrangement of the fields into radiation of gluons. Also decays due to
 347 the quantum pair creations are possible. In this way, the quark-gluon plasma is
 348 produced.

349 Interactions within the created quark-gluon plasma bring the system into
 350 the local statistical equilibrium, hence its further evolution can be described by
 351 the relativistic hydrodynamics. The hydrodynamic expansion causes the sys-
 352 tem to become more and more dilute. The phase transition from the quark-gluon
 353 plasma to the hadronic gas occurs. Further expansion causes a transition from the
 354 strongly interaction hadronic gas to weakly interacting system of hadrons which
 355 move freely to the detectors. Such decoupling of hadrons is called the *freeze-out*.
 356 The freeze-out can be divided into two phases: the chemical freeze-out and the
 357 thermal one. The *chemical freeze-out* occurs when the inelastic collisions between
 358 constituents of the hadron gas stop. As the system evolves from the chemical
 359 freeze-out to the thermal freeze-out the dominant processes are elastic collisions
 360 (such as, for example $\pi + \pi \rightarrow \rho \rightarrow \pi + \pi$) and strong decays of heavier reso-
 361 nances which populate the yield of stable hadrons. The *thermal freeze-out* is the
 362 stage of the evolution of matter, when the strongly coupled system transforms
 363 to a weakly coupled one (consisting of essentially free particles). In other words

⁴A parton is a common name for a quark and a gluon.

365 this is the moment, where the hadrons practically stop to interact. Obviously, the
 366 temperatures corresponding to the two freeze-outs satisfy the condition

$$T_{chem} > T_{therm}, \quad (1.2)$$

367 where T_{chem} (inferred from the ratios of hadron multiplicities) is the temperature
 368 of the chemical freeze-out, and T_{therm} (obtained from the investigation of the
 369 transverse-momentum spectra) is the temperature of the thermal freeze-out [10].

370 1.3.2 QGP signatures

371 The quark-gluon plasma is a very short living and unstable state of matter.
 372 One cannot investigate the properties of a plasma and confirm its existence directly.
 373 Hence, the several experimental effects were proposed as QGP signatures,
 374 some of them have been already observed in heavy ion experiments [8]. As matter
 375 created in the heavy ions collisions is supposed to behave like a fluid, one
 376 should expect appearance of collective behaviour at small transverse momenta
 377 - so called *elliptic flow* and *radial flow*. The next signal is the temperature range
 378 obtained from the measurements of *direct photons*, which gives us information,
 379 that the system created in heavy ion collisions is far above the critical temperature
 380 obtained from the LQCD calculations. The *puzzle in the di-lepton spectrum* can
 381 be explained by the modification of spectral shape of vector mesons (mostly ρ
 382 meson) in the presence of a dense medium. This presence of a medium can also
 383 shed light on the *jet quenching* phenomenon - the suppression occurrence in the
 384 high p_T domain.

385 Elliptic flow

386 In a non-central heavy ion collisions, created region of matter has an almond
 387 shape with its shorter axis in the *reaction plane* (Fig. 1.8). The pressure gradient

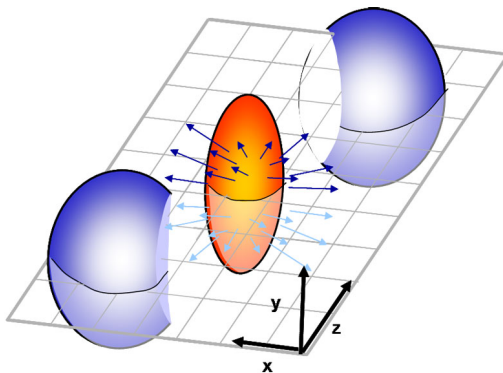


Figure 1.8: Overlapping region which is created in heavy ion collisions has an almond shape. Visible x-z plane is a *reaction plane*. The x-y plane is a *transverse plane*. The z is a direction of the beam [11].

388 is much larger in-plane rather than out-of-plane. This causes larger acceleration
 389 and transverse velocities in-plane rather than out-of-plane. Such differences can
 390 be investigated by studying the distribution of particles with respect to the reac-
 391 tion plane orientation [12]:

$$E \frac{d^3 N}{dp^3} = \frac{1}{2\pi} \frac{d^2 N}{p_T dp_T dy} (1 + 2v_1 \cos(\phi) + 2v_2 \cos(2\phi) + \dots), \quad (1.3)$$

392 where ϕ is the angle between particle transverse momentum p_T (a momentum
 393 projection on a transverse plane) and the reaction plane, N is a number of
 394 particles and E is an energy of a particle. The y variable is *rapidity* defined as:

$$y = \frac{1}{2} \ln \left(\frac{E + p_L}{E - p_L} \right), \quad (1.4)$$

395 where p_L is a longitudinal component of a momentum (parallel to the beam direc-
 396 tion). The v_n coefficients indicate the shape of a system. For the most central col-
 397 lisions ($b = 0$ - see Fig. 1.9) all coefficients vanish $\bigwedge_{n \in N_+} v_n = 0$ (the overlapping
 398 region has the spherical shape). The Fourier series elements in the parentheses
 399 in Eq. 1.3 represent different kinds of flow. The first value: "1" represents the
 400 *radial flow* - an isotropic flow in every direction. Next coefficient v_1 is responsible
 401 for *direct flow*. The v_2 coefficient is a measure of elliptic anisotropy (*elliptic flow*).
 402 The v_2 has to build up in the early stage of a collision - later the system becomes
 403 too dilute: space asymmetry and the pressure gradient vanish. Therefore the
 404 observation of elliptic flow means that the created matter was in fact a strongly
 405 interacting matter.

406 The v_2 coefficient was measured already at CERN SPS, LHC and RHIC. For
 407 the first time hydrodynamics successfully described the collision dynamics as the

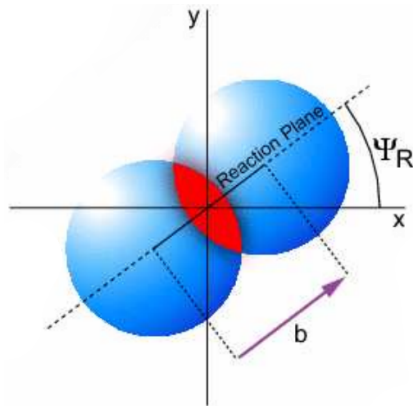


Figure 1.9: Cross-section of a heavy ion collision in a transverse plane. The b parameter is an *impact parameter* - a distance between centers of nuclei during a collision. An impact parameter is related with the centrality of a collision and a volume of the quark-gluon plasma [12].

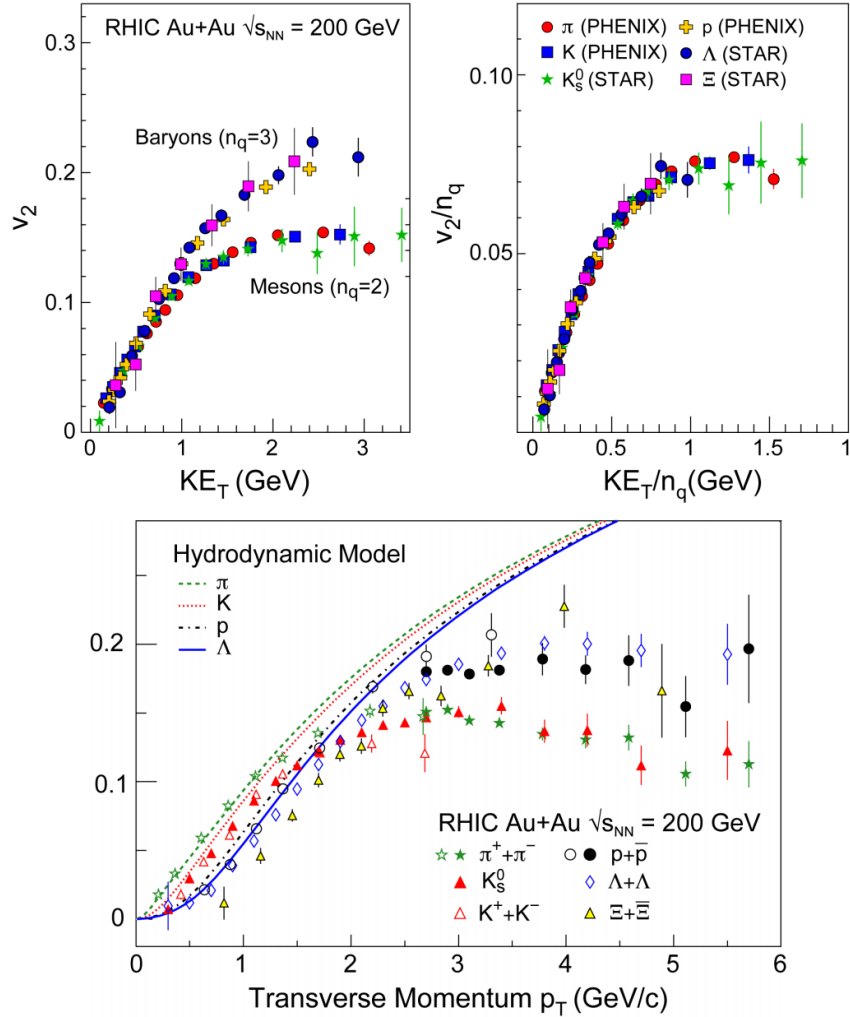


Figure 1.10: *Lower:* The elliptic flow v_2 follows the hydrodynamical predictions for an ideal fluid perfectly. Note that > 99% of all final hadrons have $p_T < 1.5 \text{ GeV}/c$. *Upper left:* The v_2 plotted versus transverse kinetic energy $KE_T = m_T - m_0 = \sqrt{p_T^2 + m_0^2} - m_0$. The v_2 follows different universal curves for mesons and baryons. *Upper right:* When scaled by the number of valence quarks, the v_2 follows the same universal curve for all hadrons and for all values of scaled transverse kinetic energy [13].

408 measured v_2 reached hydrodynamic limit (Fig. 1.10). As expected, there is a mass
 409 ordering of v_2 as a function of p_T (lower plot in the Fig. 1.10) with pions having
 410 the largest and protons the smallest anisotropy. In the upper plots in the Fig. 1.10
 411 there is a v_2 as a function of transverse kinetic energy. The left plot shows two
 412 universal trend lines for baryons and mesons. After the scaling of v_2 and the

413 kinetic energy by the number of valence quarks, all of the hadrons follow the
 414 same universal curve. Those plots show that strong collectivity is observed in
 415 heavy ion collisions.

416 **Transverse radial flow**

417 Elliptic flow described previously is caused by the pressure gradients which
 418 must also produce a more simple collective behaviour of matter - a movement
 419 inside-out, called radial flow. Particles are pushed to higher momenta and they
 420 move away from the center of the collision. A source not showing collective
 421 behaviour, like pp collisions, produces particle spectra that can be fitted by a
 422 power-law [8]:

$$\frac{1}{2\pi p_T} \frac{d^2 N}{dp_T d\eta} = C \left(1 + \frac{p_T}{p_0} \right)^{-n} . \quad (1.5)$$

423 The η variable is *pseudorapidity* defined as follows:

$$\eta = \frac{1}{2} \ln \left(\frac{p + p_L}{p - p_L} \right) = -\ln \left(\frac{\theta}{2} \right) , \quad (1.6)$$

where θ is an emission angle $\cos \theta = p_L/p$.

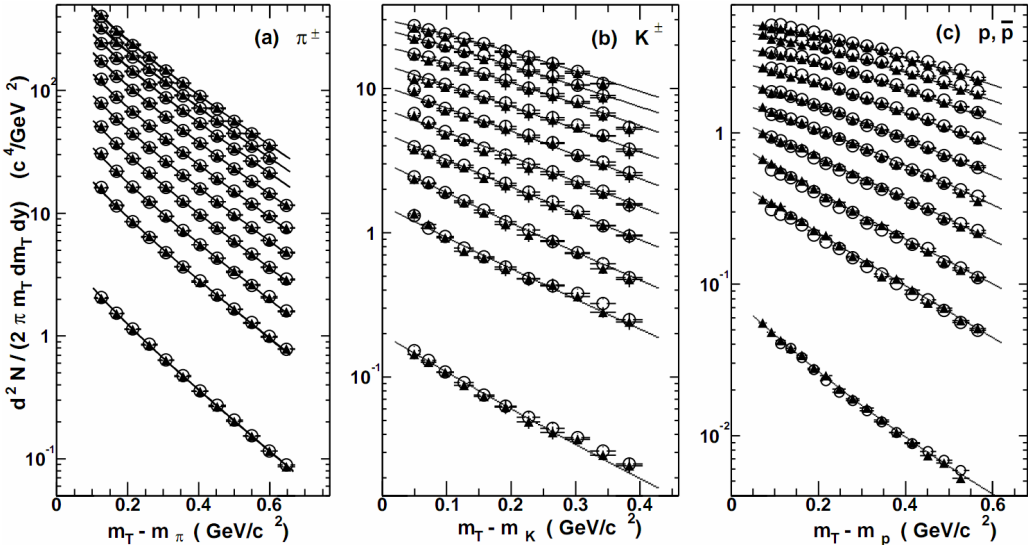


Figure 1.11: Invariant yield of particles versus transverse mass $m_T = \sqrt{p_T^2 + m_0^2}$ for π^\pm , K^\pm , p and \bar{p} at mid-rapidity for p+p collisions (bottom) and Au+Au events from 70-80% (second bottom) to 0-5% (top) centrality [14].

424
 425 The hydrodynamical expansion of a system gives the same flow velocity kick
 426 for different kinds of particles - ones with bigger masses will gain larger p_T boost.
 427 This causes increase of the yield of particles with larger transverse momenta. In

428 the invariant yield plots one can observe the decrease of the slope parameter,
 429 especially for the heavier hadrons. This is presented in the Fig. 1.11. The most
 430 affected spectra are ones of kaons (b) and protons (c). One can notice decrease
 431 of the slope parameter for heavy ion collisions (plots from second bottom to top)
 432 comparing to the proton-proton collisions (bottom ones), where no boost from
 433 radial flow should occur [8].

434 Another signature of a transverse radial flow is a dependence of HBT radii on
 435 a pair transverse momentum. Detailed description of this effect is presented in
 436 the Section 3.4.

437 Direct photons

438 The direct photons are photons, which are not coming from the final state
 439 hadrons decays. Their sources can be various interaction from charged particles
 440 created in the collision, either at the partonic or at the hadronic level. Direct
 441 photons are considered to be an excellent probe of the early stage of the collision.
 442 This is because their mean free path is very large when compared to the size of
 443 created system in the collision. Thus photons created at the early stage leave the
 444 system without suffering any interaction and retain information about this stage,
 445 in particular about its temperature.

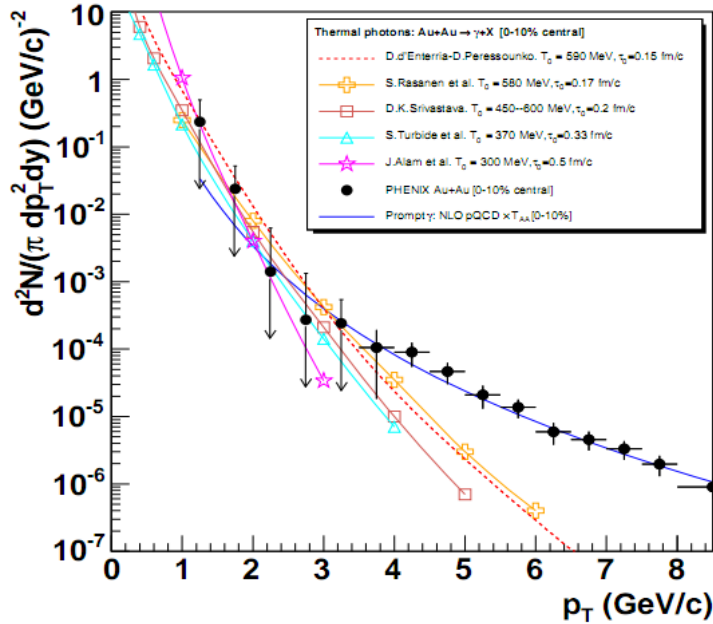


Figure 1.12: Thermal photons spectra for the central Au+Au collisions at $\sqrt{s_{NN}} = 200$ GeV computed within different hydrodynamical models compared with the pQCD calculations (solid line) and experimental data from PHENIX (black dots) [15].

One can distinguish two kinds of direct photons: *thermal* and *prompt*. Thermal photons can be emitted from the strong processes in the quark-gluon plasma involving quarks and gluons or hot hadronic matter (e.g. processes: $\pi\pi \rightarrow \rho\gamma$, $\pi\rho \rightarrow \pi\gamma$). Thermal photons can be observed in the low p_T region. Prompt photons are believed to come from “hard” collisions of initial state partons belonging to the colliding nuclei. The prompt photons can be described using the pQCD. They will dominate the high p_T region. The analysis of transverse momentum of spectra of direct photons revealed, that the temperature of the source of thermal photons produced in heavy ion collisions at RHIC is in the range 300–600 MeV (Fig. 1.12). Hence the direct photons had to come from a system whose temperature is far above from the critical temperature for QGP creation.

Puzzle in di-lepton mass spectrum

The invariant mass spectra (Fig. 1.13) of lepton pairs reveal many peaks corresponding to direct decays of various mesons into a lepton pair. The continuous background in this plot is caused by the decays of hadrons into more than two leptons (including so-called *Dalitz decays* into a lepton pair and a photon). Particular hadron decay channels, which contribute to this spectrum are shown

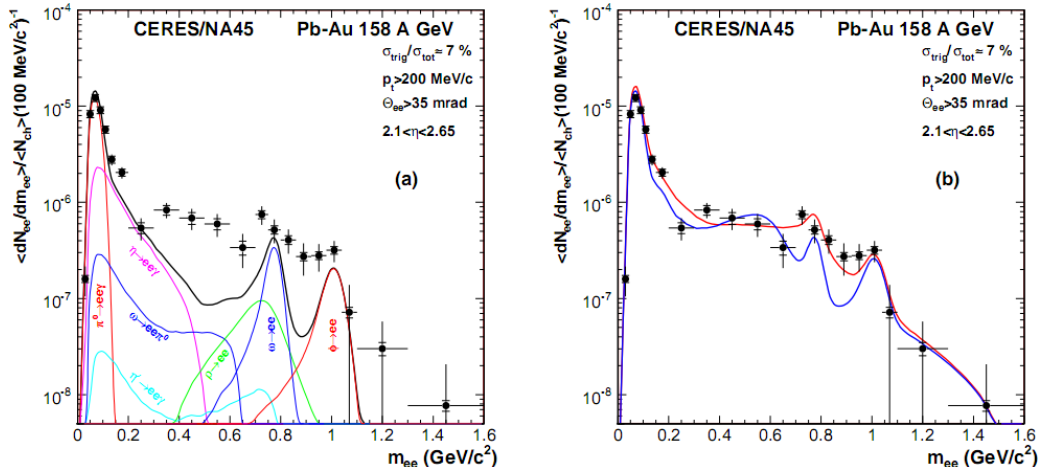


Figure 1.13: Left: Invariant mass spectrum of $e^+ - e^-$ pairs in Pb+Au collisions at 158A GeV compared to the sum coming from the hadron decays predictions. Right: The expectations coming from model calculations assuming a dropping of the ρ mass (blue) or a spread of the ρ width in the medium (red) [16].

in Fig. 1.13 with the coloured lines and their sum with the black one. The sum (called *the hadronic cocktail*) of various components describes experimental spectra coming from the simple collisions (like p+p or p+A) quite well with the statistical and systematical uncertainties [9]. This situation is different considering more complicated systems i.e. A+A. Spectra coming from Pb+Au collisions are presented on the plots in the Fig. 1.13. The “hadronic cocktail” does not describe

the data, in the mass range between the π and the ρ mesons a significant excess of electron pairs over the calculated sum is observed. Theoretical explanation of this phenomenon assumes modification of the spectral shape of vector mesons in a dense medium. Two different interpretations of this increase were proposed: a decrease of meson mass with the medium density and increase of the meson width in the dense medium. In principle, one could think of simultaneous occurrence of both effects: mass shift and resonance broadening. Experimental results coming from the CERES disfavour the mass shift hypothesis indicating only broadening of resonance peaks (Fig. 1.13b) [9].

478 Jet quenching

A jet is defined as a group of particles with close vector momenta and high energies. It has its beginning when the two partons are going in opposite directions and have energy big enough to produce new quark-antiquark pair and then radiate gluons. This process can be repeated many times and it results in two back-to-back jets of hadrons. It has been found that jets in the opposite hemisphere (*away-side jets*) show a very different pattern in d+Au and Au+Au collisions. This is shown in the azimuthal correlations in the Fig. 1.14. In d+Au collisions, like in p+p, a pronounced away-side jet appears around $\Delta\phi = \pi$, exactly opposite to the trigger jet, which is typical for di-jet events. In central Au+Au collisions the away-side jet is suppressed. When the jet has its beginning near the surface of the quark-gluon plasma, one of the jets (*near-side jet*) leaves the system almost without any interactions. This jet is visible on the correlation plot as a high peak

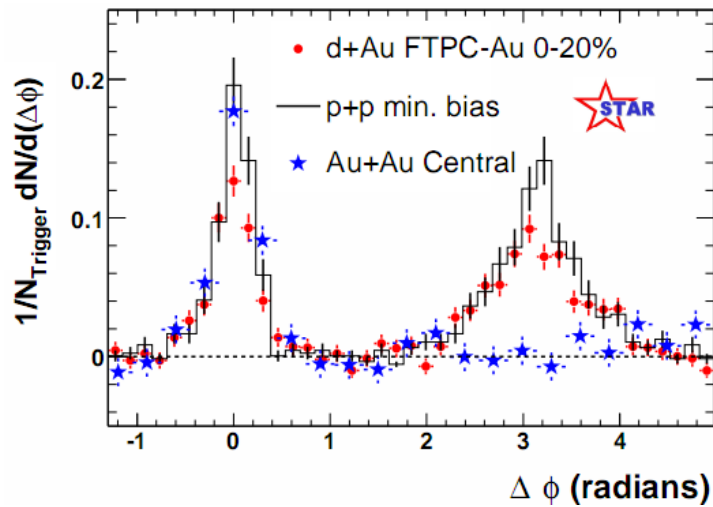


Figure 1.14: Azimuthal angle difference $\Delta\phi$ distributions for different colliding systems at $\sqrt{s_{NN}} = 200$ GeV. Transverse momentum cut: $p_T > 2$ GeV. For the Au+Au collisions the away-side jet is missing [17].

491 at $\Delta\phi = 0$. However, the jet moving towards the opposite direction has to penetrate
492 a dense medium. The interaction with the plasma causes energy dissipation
493 of particles and is visible on an azimuthal correlation plot as a disappearance of
494 the away-side jet [9].

495 **Chapter 2**

496 **Therminator model**

497 THERMINATOR [18] is a Monte Carlo event generator designed to investigate
498 the particle production in the relativistic heavy ion collisions. The functionality
499 of the code includes a generation of the stable particles and unstable resonances
500 at the chosen hypersurface model. It performs the statistical hadronization which
501 is followed by space-time evolution of particles and the decay of resonances. The
502 key element of this method is an inclusion of a complete list of hadronic reso-
503 nances, which contribute very significantly to the observables. The second version
504 of THERMINATOR [19] comes with a possibility to incorporate any shape of freeze-
505 out hypersurface and the expansion velocity field, especially those generated ex-
506 ternally with various hydrodynamic codes.

507 **2.1 (3+1)-dimensional viscous hydrodynamics**

508 Most of the relativistic viscous hydrodynamic calculations are done in
509 (2+1)-dimensions. Such simplification assumes boost-invariance of a matter
510 created in a collision. Experimental data reveals that no boost-invariant region is
511 formed in the collisions [20]. Hence, for the better description of created system
512 a (3+1)-dimensional model is required.

513 In the four dimensional relativistic dynamics one can describe a system
514 using a space-time four-vector $x^\nu = (ct, x, y, z)$, a velocity four-vector
515 $u^\nu = \gamma(c, v_x, v_y, v_z)$ and a energy-momentum tensor $T^{\mu\nu}$. The particular
516 components of $T^{\mu\nu}$ have a following meaning:

- 517 • T^{00} - an energy density,
- 518 • $cT^{0\alpha}$ - an energy flux across a surface x^α ,
- 519 • $T^{\alpha 0}$ - an α -momentum flux across a surface x^α multiplied by c ,
- 520 • $T^{\alpha\beta}$ - components of momentum flux density tensor,

521 where $\gamma = (1 - v^2/c^2)^{-1/2}$ is Lorentz factor and $\alpha, \beta \in \{1, 2, 3\}$. Using u^ν one can
 522 express $T^{\mu\nu}$ as follows [21]:

$$T_0^{\mu\nu} = (e + p)u^\mu u^\nu - pg^{\mu\nu} \quad (2.1)$$

523 where e is an energy density, p is a pressure and $g^{\mu\nu}$ is an inverse metric tensor:

$$g^{\mu\nu} = \begin{bmatrix} 1 & 0 & 0 & 0 \\ 0 & -1 & 0 & 0 \\ 0 & 0 & -1 & 0 \\ 0 & 0 & 0 & -1 \end{bmatrix}. \quad (2.2)$$

524 The presented version of energy-momentum tensor (Eq. 2.1) can be used to de-
 525 scribe dynamics of a perfect fluid. To take into account influence of viscosity,
 526 one has to apply the following corrections coming from shear $\pi^{\mu\nu}$ and bulk Π
 527 viscosities [22]:

$$T^{\mu\nu} = T_0^{\mu\nu} + \pi^{\mu\nu} + \Pi(g^{\mu\nu} - u^\mu u^\nu). \quad (2.3)$$

528 The stress tensor $\pi^{\mu\nu}$ and the bulk viscosity Π are solutions of dynamical equa-
 529 tions in the second order viscous hydrodynamic framework [21]. The compari-
 530 son of hydrodynamics calculations with the experimental results reveal, that the
 531 shear viscosity divided by entropy η/s has to be small and close to the AdS/CFT
 532 estimate $\eta/s = 0.08$ [22, 23]. The bulk viscosity over entropy value used in calcu-
 533 lations is $\zeta/s = 0.04$ [22].

534 When using $T^{\mu\nu}$ to describe system evolving close to local thermodynamic
 535 equilibrium, relativistic hydrodynamic equations in a form of:

$$\partial_\mu T^{\mu\nu} = 0 \quad (2.4)$$

536 can be used to describe the dynamics of the local energy density, pressure and
 537 flow velocity.

538 Hydrodynamic calculations are starting from the Glauber¹ model initial con-
 539 ditions. The collective expansion of a fluid ends at the freeze-out hypersurface.
 540 That surface is usually defined as a constant temperature surface, or equivalently
 541 as a cut-off in local energy density. The freeze-out is assumed to occur at the
 542 temperature $T = 140$ MeV.

543 2.2 Statistical hadronization

544 Statistical description of heavy ion collision has been successfully used to
 545 quantitatively describe the *soft* physics, i.e. the regime with the transverse mo-
 546 mentum not exceeding 2 GeV. The basic assumption of the statistical approach of
 547 evolution of the quark-gluon plasma is that at some point of the space-time evol-
 548 ution of the fireball, the thermal equilibrium is reached. When the system is in the

¹The Glauber Model is used to calculate “geometrical” parameters of a collision like an impact parameter, number of participating nucleons or number of binary collisions.

549 thermal equilibrium the local phase-space densities of particles follow the Fermi-
 550 Dirac or Bose-Einstein statistical distributions. At the end of the plasma expan-
 551 sion, the freeze-out occurs. The freeze-out model incorporated in THERMINATOR
 552 assumes, that chemical and thermal freeze-outs occur at the same time.

553 **2.2.1 Cooper-Frye formalism**

554 The result of the hydrodynamic calculations is the freeze-out hyper-
 555 surface Σ^μ . A three-dimensional element of the surface is defined as [19]

$$556 \quad d\Sigma_\mu = \epsilon_{\mu\alpha\beta\gamma} \frac{\partial x^\alpha}{\partial \alpha} \frac{\partial x^\beta}{\partial \beta} \frac{\partial x^\gamma}{\partial \gamma} d\alpha d\beta d\gamma, \quad (2.5)$$

557 where $\epsilon_{\mu\alpha\beta\gamma}$ is the Levi-Civita tensor and the variables $\alpha, \beta, \gamma \in \{1, 2, 3\}$ are used
 558 to parametrize the three-dimensional freeze-out hypersurface in the Minkowski
 559 four-dimensional space. The Levi-Civita tensor is equal to 1 when the indices
 560 form an even permutation (eg. ϵ_{0123}), to -1 when the permutation is odd (e.g.
 561 ϵ_{2134}) and has a value of 0 if any index is repeated. Therefore [19],

$$562 \quad d\Sigma_0 = \begin{vmatrix} \frac{\partial x}{\partial \alpha} & \frac{\partial x}{\partial \beta} & \frac{\partial x}{\partial \gamma} \\ \frac{\partial y}{\partial \alpha} & \frac{\partial y}{\partial \beta} & \frac{\partial y}{\partial \gamma} \\ \frac{\partial z}{\partial \alpha} & \frac{\partial z}{\partial \beta} & \frac{\partial z}{\partial \gamma} \end{vmatrix} d\alpha d\beta d\gamma \quad (2.6)$$

562 and the remaining components are obtained by cyclic permutations of t, x, y
 563 and z .

One can obtain the number of hadrons produced on the hypersurface Σ^μ from
 the Cooper-Frye formalism. The following integral yields the total number of
 created particles [19]:

$$564 \quad N = (2s + 1) \int \frac{d^3 p}{(2\pi)^3 E_p} \int d\Sigma_\mu p^\mu f(p_\mu u^\mu), \quad (2.7)$$

564 where $f(p_\mu u^\mu)$ is the phase-space distribution of particles (for stable ones and res-
 565 onances). One can simply derive from Eq. 2.7, the dependence of the momentum
 566 density [24]:

$$567 \quad E \frac{d^3 N}{dp^3} = \int d\Sigma_\mu f(p_\mu u^\mu) p^\mu. \quad (2.8)$$

567 The momentum distribution f contains non-equilibrium corrections:

$$568 \quad f = f_0 + \delta f_{shear} + \delta f_{bulk}, \quad (2.9)$$

568 where

$$569 \quad f_0(p_\mu u^\mu) = \left\{ \exp \left[\frac{p_\mu u^\mu - (B\mu_B + I_3\mu_{I_3} + S\mu_S + C\mu_C)}{T} \right] \pm 1 \right\}^{-1}. \quad (2.10)$$

569 In case of fermions, in the Eq. 2.10 there is a plus sign and for bosons, minus
 570 sign respectively. The thermodynamic quantities appearing in the $f_0(\cdot)$ are T -
 571 temperature, μ_B - baryon chemical potential, μ_{I_3} - isospin chemical potential, μ_S
 572 - strange chemical potential, μ_C - charmed chemical potential and the s is a spin of
 573 a particle. The hydrodynamic calculations yield the flow velocity at freeze-out as
 574 well as the stress and bulk viscosity tensors required to calculate non-equilibrium
 575 corrections to the momentum distribution used in Eq. 2.7. The term coming from
 576 shear viscosity has a form [22]

$$\delta f_{shear} = f_0(1 \pm f_0) \frac{1}{2T^2(e + p)} p^\mu p^\nu \pi_{\mu\nu} \quad (2.11)$$

577 and bulk viscosity

$$\delta f_{bulk} = C f_0(1 \pm f_0) \left(\frac{(u^\mu p_\mu)^2}{3u^\mu p_\mu} - c_s^2 u^\mu p_\mu \right) \Pi \quad (2.12)$$

578 where c_s is sound velocity and

$$\frac{1}{C} = \frac{1}{3} \frac{1}{(2\pi)^3} \sum_{hadrons} \int d^3 p \frac{m^2}{E} f_0(1 \pm f_0) \left(\frac{p^2}{3E} - c_s^2 E \right). \quad (2.13)$$

579 2.3 Events generation procedure

580 The equations presented in the previous section are directly used in the
 581 THERMINATOR to generate the primordial hadrons (created during freeze-out)
 582 with the Monte-Carlo method. This procedure consists of 3 main steps, where
 583 the first two are performed only once per given parameter set. After the
 584 generation of primordial particles, the cascade decay of unstable resonances is
 585 performed.

586 Determination of a maximum of an integrand

587 In order to generate particles through a Monte Carlo method, the maximum
 588 value of the distribution in the right-hand-side of Eq. 2.7 must be known. To find
 589 this number, THERMINATOR performs a generation of a sample consisting of a
 590 large number of particles. For each particle the value of a distribution is cal-
 591 culated and the maximum value f_{max} of the sample is stored. A large enough
 592 sample of particles guarantees that f_{max} found in this procedure is a good es-
 593 timate of the maximum value of a distribution in Eq. 2.7. This maximum value
 594 depends on a particle type and values of parameters, but does not change from
 595 event to event, hence this procedure is performed once, at the beginning of the
 596 events generation [18].

597 **Multiplicity calculation**

598 In order to generate events, a multiplicity of each particle must be known.
 599 The multiplicities are obtained through a numerical integration of distribution
 600 functions (Eq. 2.7) in the given integration ranges determined by the model para-
 601 meters. The multiplicities also depend only on the model parameters and they
 602 are also only calculated once at the beginning of the event generation [18].

603 **Events and particles generation**

604 Each of the events produced by THERMINATOR are generated separately. At
 605 first, the multiplicities for each of particle type are generated as random numbers
 606 from a Poisson distribution, with the mean being the average particle multipli-
 607 city determined in the previous step. Then the program proceeds to generate
 608 particles from the heaviest to the lightest particle type. In essence, this procedure
 609 is a generation of the set of six random numbers: three components of particle's
 610 momentum (p_x, p_y, p_z) and three parameters providing space-time coordinates
 611 on a freeze-out hypersurface (ζ, ϕ_s, θ). Event generation procedure is based on
 612 von Neumann's acceptance-rejection algorithm. Firstly, the integrand in Eq. 2.7
 613 is calculated using given set of numbers. Subsequently, a random number from
 614 uniform distribution over $[0; f_{max}]$ is compared to the value of integrand. If it
 615 is lower, then the set of numbers is stored as actual particle. If this condition
 616 was not satisfied, a new set is generated. This procedure is repeated until the
 617 determined number of particles of each kind is generated. At this point all prim-
 618 ordial particles (stable and resonances) have been generated and stored in the
 619 event [18].

620 **Decays of unstable particles**

621 In the next step of event generation, a simulation of decays of unstable res-
 622 onances is performed. A particle is considered as unstable when it has non-zero
 623 width Γ defined in the input files of THERMINATOR. The decays proceed sequen-
 624 tially from the heaviest particles to the lightest. Unstable products of decays are
 625 added to the particles generated in the current event and are processed in the
 626 subsequent steps. If a particle has several decay channels, one of them is selec-
 627 ted randomly with the appropriate probability corresponding to the branching
 628 ratio provided in the input files. THERMINATOR in the hadronic cascade process
 629 performs two-body and three-body decays.

630 At the beginning of the cascade decay, the lifetime τ of a particle with mass
 631 M , moving with the four-momentum p^μ , is generated randomly according to the
 632 exponential decay law $\exp(-\Gamma\tau)$. When the lifetime is known, the point of its
 633 decay is calculated as [18]:

$$x_{decay}^\mu = x_{origin}^\mu + \frac{p^\mu}{M}\tau, \quad (2.14)$$

634 where x_{origin}^μ is a space-time position, where the unstable particle was generated.
 635 At the x_{decay}^μ point decay occurs and daughter particles with energies and mo-
 636 ments determined by the conservation laws are generated. Fig. 2.1 illustrates the
 cascade decay process [18].

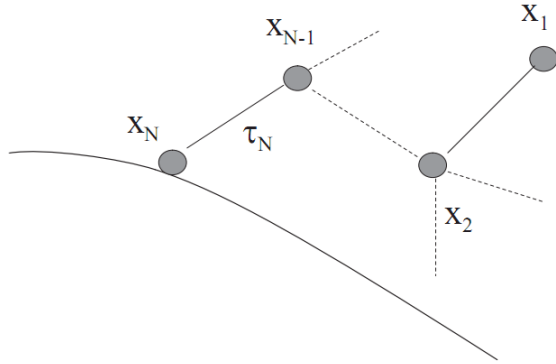


Figure 2.1: The cascade decay in the single freeze-out model. An unstable resonance x_N is formed at the freeze-out hypersurface and travels for the time τ_N depending on its lifetime and decays. If the products are also resonances (x_{N-1} , x_2) they decay further until the stable particles are formed (x_1) [18].

638 **Chapter 3**

639 **Particle interferometry**

640 Two-particle interferometry (also called *femtoscopy*) gives a possibility to
641 investigate space-time characteristics of the particle-emitting source created
642 in heavy ion collisions. Through the study of particle correlations, their
643 momentum distributions can be used to obtain information about the spatial
644 extent of the created system. Using this method, one can measure sizes of the
645 order of 10^{-15} m and time of the order of 10^{-23} s.

646 **3.1 HBT interferometry**

647 In the 1956 Robert Hanbury Brown and Richard Q. Twiss proposed a method
648 which allowed to investigate angular dimensions of stars through analysis of
649 interference between photons. They performed a measurement of the intensity
650 of a beam of light coming from a star using two separated detectors. In a sig-
651 nal plotted as a function of distance between detectors an interference effect was
652 observed, revealing a positive correlation, despite the fact that no phase inform-
653 ation was collected. Hanbury, Brown and Twiss used this interference signal to
654 calculate the angular size of a star with the excellent resolution. This method was
655 designed to be used in astronomy, however HBT interferometry can be used also
656 to measure extent of any emitting source. Therefore it was adapted to heavy ion
657 collisions to investigate dimensions of a particle-emitting source [8].

658 **3.2 Theoretical approach**

659 Intensity interferometry in heavy ion physics uses similar mathematical form-
660 alism as the astronomy HBT measurement. The difference between them is that
661 femtoscopy uses a two-particle relative momentum and yields the space-time
662 picture of a source, whereas the latter method uses the distance between detect-
663 ors to calculate angular size of the star.

664 **3.2.1 Conventions used**

665 In heavy ion collisions to describe particular directions, components of mo-
 666 mentum and location of particles, one uses naming convention called the Bertsch-
 Pratt coordinate system. This system is presented in the Fig. 3.1. The three dir-

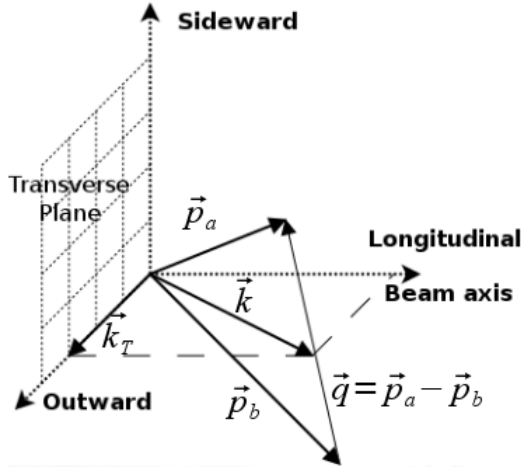


Figure 3.1: Bertsch-Pratt direction naming convention used in heavy ion collision.

667
 668 ections are called *longitudinal*, *outward* and *sideward*. The longitudinal direction
 669 is parallel to the beam axis. The plane perpendicular to the beam axis is called
 670 a *transverse plane*. A projection of a particle pair momentum $\mathbf{k} = (\mathbf{p}_a + \mathbf{p}_b)/2$
 671 on a transverse plane (a *transverse momentum* \mathbf{k}_T) determines *outward* direction:
 672 $(\mathbf{k})_{out} = \mathbf{k}_T$. A direction perpendicular to the longitudinal and outward is called
 673 *sideward*.

674 A particle pair is usually described using two coordinate systems. The first
 675 one, *Longitudinally Co-Moving System* (LCMS) is moving along the particle pair
 676 with the longitudinal direction, in other words, the pair longitudinal momentum
 677 vanishes: $(\mathbf{p}_a)_{long} = -(\mathbf{p}_b)_{long}$. The second system is called *Pair Rest Frame* (PRF).
 678 In the PRF the centre of mass rests: $\mathbf{p}_a = -\mathbf{p}_b$. Variables which are expressed in
 679 the PRF are marked with a star (e.g. \mathbf{k}^*).

The transition of space-time coordinates from LCMS to PRF is simply
 a boost along the outward direction, with the transverse velocity of the
 pair $\beta_T = (\mathbf{v}/c)_{out}$ [25]:

$$r_{out}^* = \gamma_T(r_{out} - \beta_T \Delta t) \quad (3.1)$$

$$r_{side}^* = r_{side} \quad (3.2)$$

$$r_{long}^* = r_{long} \quad (3.3)$$

$$\Delta t^* = \gamma_T(\Delta t - \beta_T r_{out}), \quad (3.4)$$

680 where $\gamma_T = (1 - \beta_T^2)^{-1/2}$ is the Lorentz factor. However, in calculations performed

in this work the equal time approximation is used, which assumes that particles in a pair were produced at the same time in PRF - the Δt^* is neglected.

The most important variables used to describe particle pair are their total momentum $\mathbf{P} = \mathbf{p}_a + \mathbf{p}_b$ and relative momentum $\mathbf{q} = \mathbf{p}_a - \mathbf{p}_b$. In the PRF one has $\mathbf{q} = 2\mathbf{k}^*$, where \mathbf{k}^* is a momentum of the first particle in PRF.

3.2.2 Two particle wave function

Let us consider two identical particles with momenta \mathbf{p}_1 and \mathbf{p}_2 emitted from space points \mathbf{x}_1 and \mathbf{x}_2 . Those emitted particles can be treated as two incoherent waves. If the particles are identical, they are also indistinguishable, therefore one

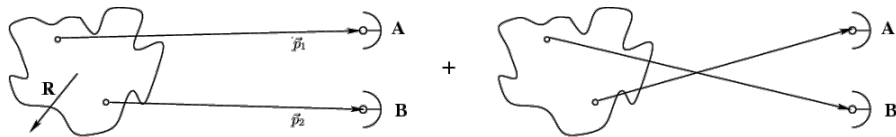


Figure 3.2: The pair wave function is a superposition of all possible states. In case of particle interferometry it includes two cases: particles with momenta p_1, p_2 registered by detectors A, B and p_1, p_2 registered by B, A respectively.

has also take into account the scenario, where the particle with momentum \mathbf{p}_1 is emitted from \mathbf{x}_2 and particle \mathbf{p}_2 from \mathbf{x}_1 (Fig. 3.2). In such case, the wave function describing behaviour of a pair has to contain both components [8]:

$$\Psi_{ab}(\mathbf{q}) = \frac{1}{\sqrt{2}} [\exp(-i\mathbf{p}_1\mathbf{x}_1 - i\mathbf{p}_2\mathbf{x}_2) \pm \exp(-i\mathbf{p}_2\mathbf{x}_1 - i\mathbf{p}_1\mathbf{x}_2)] . \quad (3.5)$$

A two particle wave function of identical bosons is symmetric ("+" sign in Eq. 3.5) and in case of identical fermions - antisymmetric ("-" sign). This anti-symmetrization or symmetrization implies the correlation effect coming from the Fermi-Dirac or Bose-Einstein statistics accordingly.

To provide full description of a system consisting of two charged hadrons, one has to include in the wave function besides quantum statistics also Coulomb and strong Final State Interactions. The aim of this work is an analysis of femtoscopic radii proportional to the inverse of a width of a correlation function (for detailed description see Section 3.2.4). Since we are not interested in the direct comparison of experimental correlation functions with their analytical forms, the following simplification can be made. A width of identical particles correlation function is determined by effects coming from quantum statistics, hence one can ignore influence of Final State Interactions, which in this case is small. Taking into account only quantum statistics can reduce complexity of calculations and save computation time.

708 **3.2.3 Source emission function**

709 To describe particle emitting source, one uses a single emission function [25]:

710

$$S_A(\mathbf{x}_1, \mathbf{p}_1) = \int S(\mathbf{x}_1, \mathbf{p}_1, \mathbf{x}_2, \mathbf{p}_2, \dots, \mathbf{x}_N, \mathbf{p}_N) d\mathbf{x}_2 d\mathbf{p}_2 \dots d\mathbf{x}_N d\mathbf{p}_N \quad (3.6)$$

711 and a two-particle one:

$$S_{AB}(\mathbf{x}_1, \mathbf{p}_1, \mathbf{x}_2, \mathbf{p}_2) = \int S(\mathbf{x}_1, \mathbf{p}_1, \mathbf{x}_2, \mathbf{p}_2, \dots, \mathbf{x}_N, \mathbf{p}_N) d\mathbf{x}_3 d\mathbf{p}_3 \dots d\mathbf{x}_N d\mathbf{p}_N . \quad (3.7)$$

712 Emission function $S(\cdot)$ can be interpreted as a probability to emit a particle, or
 713 a pair of particles from a given space-time point with a given momentum. In
 714 principle, the source emission function should encode all physics aspects of the
 715 particle emission process i.e. the symmetrization for bosons and fermions, as
 716 well as the two-body and many body Final State Interactions. Instead of this,
 717 one assume that each particle's emission process is independent - the interac-
 718 tion between final-state particles after their creation is independent from their
 719 emission process. The assumption of this independence allows to construct two-
 720 particle emission function from single particle emission functions via a convolu-
 721 tion [25]:

$$S(\mathbf{k}^*, \mathbf{r}^*) = \int S_A(\mathbf{p}_1, \mathbf{x}_1) S_B(\mathbf{p}_2, \mathbf{x}_2) \delta \left[\mathbf{k}^* - \frac{\mathbf{p}_1 + \mathbf{p}_2}{2} \right] \delta [\mathbf{r}^* - (\mathbf{x}_1 + \mathbf{x}_2)] \times d^4 \mathbf{x}_1 d^4 \mathbf{x}_2 d^4 \mathbf{x}_1 d^3 \mathbf{p}_1 d^3 \mathbf{p}_2 \quad (3.8)$$

722 In case of identical particles, ($S_A = S_B$) several simplifications can be made. A
 723 convolution of the two identical Gaussian distributions is also a Gaussian distri-
 724 bution with σ multiplied by $\sqrt{2}$. Femtoscopy can give information only about
 725 two-particle emission function, but when considering Gaussian distribution as
 726 a source function in Eq. 3.8, one can obtain a σ of a single emission function
 727 from a two-particle emission function. The Eq. 3.8 is not reversible - an inform-
 728 ation about $S_A(\cdot)$ cannot be derived from $S_{AB}(\cdot)$. An exception from this rule
 729 is a Gaussian source function, hence it is often used in femtoscopic calculations.
 730 Considering pairs of identical particles, an emission function is assumed to be
 731 described by the following equation in the Pair Rest Frame [25]:

$$S_{1D}^{PRF}(\mathbf{r}^*) = \exp \left(-\frac{r_{out}^{*2} + r_{side}^{*2} + r_{long}^{*2}}{4R_{inv}^2} \right) . \quad (3.9)$$

To change from the three-dimensional variables to the one-dimensional variable
 one requires introduction of the proper Jacobian r^{*2} .

$$S_{1D}^{PRF}(r^*) = r^{*2} \exp \left(-\frac{r^{*2}}{4R_{inv}^2} \right) . \quad (3.10)$$

732 The “4” in the denominator before the “standard deviation” R_{inv} in the Gaussian
 733 distribution comes from the convolution of the two Gaussian distributions,
 734 which multiplies the R_{inv} by a factor of $\sqrt{2}$.

A more complex form of emission function was used by all RHIC and SPS experiments in identical pion femtoscopy:

$$S_{3D}^{LCMS}(\mathbf{r}) = \exp \left(-\frac{r_{out}^2}{4R_{out}^2} - \frac{r_{side}^2}{4R_{side}^2} - \frac{r_{long}^2}{4R_{long}^2} \right). \quad (3.11)$$

735 The main difference of this source function is that it has three different and inde-
 736 pendent widths R_{out} , R_{side} , R_{long} and they are defined in the LCMS, not in PRF.
 737 Unlike in PRF, in LCMS an equal-time approximation is not used. For identical
 738 particles this is not a problem - only Coulomb interaction inside a wave function
 739 depends on Δt .

740 Relationship between one-dimensional and three-dimensional source sizes

741 Up to now, most of femtoscopic measurements were limited only to averaged
 742 source size R_{av}^L (the letter “L” in superscript stands for LCMS):

$$S_{1D}^{LCMS}(\mathbf{r}) = \exp \left(-\frac{r_{out}^2 + r_{side}^2 + r_{long}^2}{2R_{av}^L} \right). \quad (3.12)$$

743 The relationship between between $S_{1D}^{LCMS}(\cdot)$ and $S_{3D}^{LCMS}(\cdot)$ is given by:

$$S_{3D}^{LCMS}(r) = \int \exp \left(-\frac{r_{out}^2}{2R_{out}^L} - \frac{r_{side}^2}{2R_{side}^L} - \frac{r_{long}^2}{2R_{long}^L} \right) \times \delta \left(r - \sqrt{r_{out}^2 + r_{side}^2 + r_{long}^2} \right) dr_{out} dr_{side} dr_{long}. \quad (3.13)$$

744 The one-dimensional source size corresponding to the three-dimensional one can
 745 be approximated by the following form:

$$S_{1D}^{LCMS}(r) = r^2 \exp \left(-\frac{r^2}{2R_{av}^L} \right). \quad (3.14)$$

746 The equation above assumes that $R_{out}^L = R_{side}^L = R_{long}^L$ hence $R_{av}^L = R_{out}^L$. If this
 747 condition is not satisfied, one can not give explicit mathematical relation between
 748 one-dimensional and three-dimensional source sizes. However, for realistic val-
 749 ues of R (i.e. for similar values of R_{out} , R_{side} , R_{long}), the S_{3D}^{LCMS} from Eq. 3.13 is
 750 not very different from Gaussian distribution and can be well approximated by
 751 Eq. 3.13.

752 A deformation of an averaged source function in case of big differences in
 753 R_{out} , R_{side} , R_{long} is presented in the Fig. 3.3. A three-dimensional Gaussian dis-
 754 tribution with varying widths was averaged into one-dimensional function using

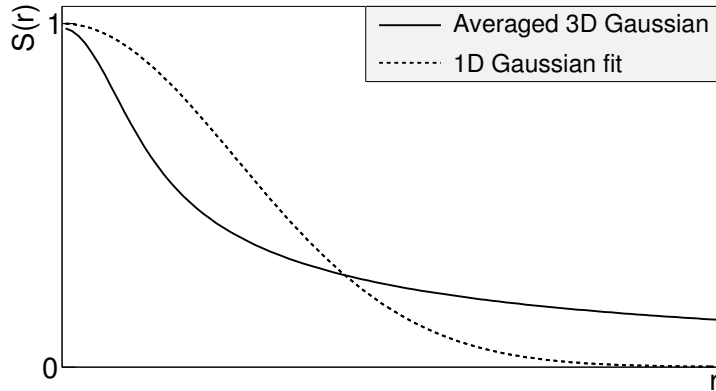


Figure 3.3: An averaged three-dimensional Gaussian source function with different widths was averaged into one-dimensional function. To illustrate deformations, one-dimensional Gaussian distribution was fitted.

the Eq. 3.13. Afterwards, an one-dimensional Gaussian distribution was fitted.
One can notice a heavy tail of an averaged distribution in long r region, which
makes an approximation using one-dimensional distribution in this case quite
inaccurate.

Using Eq. 3.13 and Eq. 3.14 one can obtain a relation between one-dimensional width and the three-dimensional ones. Through numerical calculations one can find the following approximate relation [25]:

$$R_{av}^L = \sqrt{\left(R_{out}^{L^2} + R_{side}^{L^2} + R_{long}^{L^2}\right)/3}. \quad (3.15)$$

This equation does not depend on the pair velocity, hence it is valid in the LCMS and PRF.

3.2.4 Analytical form of a correlation function

The fundamental object in a particle interferometry is a correlation function. The correlation function is defined as:

$$C(\mathbf{p}_a, \mathbf{p}_b) = \frac{P_2(\mathbf{p}_a, \mathbf{p}_b)}{P_1(\mathbf{p}_a)P_1(\mathbf{p}_b)}, \quad (3.16)$$

where P_2 is a conditional probability to observe a particle with momentum \mathbf{p}_b if particle with momentum \mathbf{p}_a was also observed. A P_1 is a probability to observe a particle with a given momentum. The relationship between source emission function, pair wave function and the correlation function is described by the following equation:

$$C(\mathbf{p}_1, \mathbf{p}_2) = \int S_{AB}(\mathbf{p}_1, \mathbf{x}_1, \mathbf{p}_2, \mathbf{x}_2) |\Psi_{AB}|^2 d^4\mathbf{x}_1 d^4\mathbf{x}_2 \quad (3.17)$$

Substituting the one-dimensional emission function (Eq. 3.10) into the integral above yields the following form of correlation function in PRF:

$$C(q) = 1 + \lambda \exp(-R_{inv}^2 q^2) \quad (3.18)$$

where q is a momentum difference between two particles. When using the three-dimensional emission function (Eq. 3.11) one gets the following correlation function defined in the LCMS:

$$C(\mathbf{q}) = 1 + \lambda \exp(-R_{out}^2 q_{out}^2 - R_{side}^2 q_{side}^2 - R_{long}^2 q_{long}^2) \quad (3.19)$$

where q_{out} , q_{side} , q_{long} are \mathbf{q} components in the outward, sideward and longitudinal direction. The λ parameter in the equations above determines correlation strength. The lambda parameter has values in the range $\lambda \in [-0.5, 1]$ and it depends on a pair type. In case of pairs of identical bosons (like $\pi\pi$ or KK) the lambda parameter $\lambda \rightarrow 1$. For identical fermions (e.g. $p-p$) $\lambda \rightarrow -0.5$. Values of λ observed experimentally are lower than 1 (for bosons) and greater than -0.5 (for fermions). There are few explanations to this effect: detector efficiencies, inclusion of misidentified particles in a used sample or inclusion of non-correlated pairs (when one or both particles come from e.g. long-lived resonance). The analysis carried out in this work uses data from a model, therefore the detector efficiency and particle purity is not taken into account [25].

3.2.5 Spherical harmonics decomposition of a correlation function

Results coming from an analysis using three-dimensional correlation function in Cartesian coordinates are quite difficult to visualize. To do that, one usually performs a projection into one dimension in outward, sideward and longitudinal directions. One may loose important information about a correlation function in this procedure, because it gives only a limited view of the full three-dimensional structure. Recently, a more advanced way of presenting correlation function - a spherical harmonics decomposition, was proposed. The three-dimensional correlation function is decomposed into an infinite set of components in a form of one-dimensional histograms $C_l^m(q)$. In this form, a correlation function is defined as a sum of a series [26]:

$$C(\mathbf{q}) = \sum_{l,m} C_l^m(q) Y_l^m(\theta, \phi), \quad (3.20)$$

where $Y_l^m(\theta, \phi)$ is a spherical harmonic function. Spherical harmonics are an orthogonal set of solutions to the Laplace's equation in spherical coordinates. Hence, in this approach, a correlation function is defined as a function of q , θ and ϕ . To obtain C_l^m coefficients in the series, one has to calculate the following integral:

$$C_l^m(q) = \int_{\Omega} C(q, \theta, \phi) Y_l^{m*}(\theta, \phi) d\Omega, \quad (3.21)$$

796 where Ω is a full solid angle.

Spherical harmonics representation has several important advantages. The main one is that it requires less statistics than traditional analysis performed in Cartesian coordinates. Another one is that it encodes full three-dimensional information in a set of one-dimensional plots. In principle it does not have to be an advantage, because full description of a correlation function requires infinite number of l, m components. But it so happens that the intrinsic symmetries of a pair distribution in a femtoscopic analysis result in most of the components to vanish. For the identical particles correlation functions, all coefficients with odd values of l and m disappear. It has also been shown, that the most significant portion of femtoscopic data is stored in the components with the lowest l values. It is expected that, the main femtoscopic information is contained in the following components [25]:

$$C_0^0 \rightarrow R_{LCMS}, \quad (3.22)$$

$$\Re C_2^0 \rightarrow \frac{R_T}{R_{long}}, \quad (3.23)$$

$$\Re C_2^2 \rightarrow \frac{R_{out}}{R_{side}}, \quad (3.24)$$

797 where $R_{LCMS} = \sqrt{(R_{out}^2 + R_{side}^2 + R_{long}^2)/3}$ and $R_T = \sqrt{(R_{out}^2 + R_{side}^2)/2}$.

798 The C_0^0 is sensitive to the overall size of a correlation function. The $\Re C_2^0$ carries
 799 the information about the ratio of the transverse to the longitudinal radii, due
 800 to its $\cos^2(\theta)$ weighting in Y_2^0 . The component $\Re C_2^2$ with its $\cos^2(\phi)$ weighting
 801 encodes the ratio between outward and sideward radii. Thus, the spherical har-
 802 monics method allows to obtain and analyze full three-dimensional femtoscopic
 803 information from a correlation function [25].

804 3.3 Experimental approach

805 The correlation function is defined as a probability to observe two particles
 806 together divided by the product of probabilities to observe each of them sepa-
 807 rately (Eq. 3.16). Experimentally this is achieved by dividing two distributions
 808 of relative momentum of pairs of particles coming from the same event and the
 809 equivalent distribution of pairs where each particle is taken from different colli-
 810 sions. In this way, one obtains not only femtoscopic information but also all other
 811 event-wide correlations. This method is useful for experimentalists to estimate
 812 the magnitude of non-femtoscopic effects. There exists also a different approach,
 813 where two particles in pairs in the second distribution are also taken from the
 814 same event. The second method gives only information about physical effects
 815 accessible via femtoscopy. The aim of this work is a study of effects coming from
 816 two particle interferometry, hence the latter method was used.

817 In order to calculate experimental correlation function, one uses the follow-
 818 ing approach. One has to construct two histograms: the *numerator* N and the

819 denominator D with the particle pairs momenta, where particles are coming from
 820 the same event. Those histograms can be one-dimensional (as a function of $|\mathbf{q}|$),
 821 three dimensional (a function of three components of \mathbf{q} in LCMS) or a set of one-
 822 dimensional histogram representing components of the spherical harmonic de-
 823 composition of the distribution. The second histogram, D is filled for each pair
 824 with the weight 1.0 at a corresponding relative momentum $\mathbf{q} = 2\mathbf{k}^*$. The first one,
 825 N is filled with the same procedure, but the weight is calculated as $|\Psi_{ab}(\mathbf{r}^*, \mathbf{k}^*)|^2$.
 826 A division N/D gives the correlation function C . This procedure can be simply
 827 written as [25]:

$$C(\mathbf{k}^*) = \frac{N}{D} = \frac{\sum_{n_i \in D} \delta(\mathbf{k}_i^* - \mathbf{k}^*) |\Psi_{ab}(\mathbf{r}_i^*, \mathbf{k}_i^*)|^2}{\sum_{n_i \in D} \delta(\mathbf{k}_i^* - \mathbf{k}^*)} . \quad (3.25)$$

The D histogram represents the set of all particle pairs used in calculations.
 The n_i is a pair with the its relative momentum \mathbf{k}_i^* and relative separation \mathbf{r}_i^* .
 Mathematically, the procedure of calculating the Eq. 3.25 is equivalent to a
 calculation of an integral in Eq. 3.17 through a Monte-Carlo method. The wave
 function used in Eq. 3.25 has one of the following forms:

$$|\Psi_{\pi\pi}(\mathbf{r}^*, \mathbf{k}^*)|^2 = |\Psi_{KK}(\mathbf{r}^*, \mathbf{k}^*)|^2 = 1 + \cos(2\mathbf{k}^* \mathbf{r}^*) , \quad (3.26)$$

$$|\Psi_{pp}(\mathbf{r}^*, \mathbf{k}^*)|^2 = 1 - \frac{1}{2} \cos(2\mathbf{k}^* \mathbf{r}^*) . \quad (3.27)$$

828 The first one is used in case of bosons, and the latter one is for identical fermions.
 829 A wave function for pair of spin-1/2 fermions (Eq. 3.27) is a superposition of two
 830 possible states: singlet state (with spin equal to 0 and one eigenstate) and triplet
 831 state (with spin equal to 1 and three possible eigenstates). For a singlet state, a
 832 wave function is symmetric, and for triplet state, it is antisymmetric. In other
 833 words the $|\Psi_{pp}|^2$ encodes correlation coming from Bose-Einstein statistics (with
 834 weight 1/4) and anti-correlation from Fermi-Dirac distribution (with weight 3/4).

835 3.4 Scaling of femtoscopy radii

836 A particle interferometry formalism presented in the previous sections as-
 837 sumes that particle emitting source is static. This is not the case in heavy ion
 838 collisions at LHC. An existence of transverse radial and elliptic flow suggest that
 839 created system is dynamic. To address this issue, a concept of *lengths of homogen-*
 840 *eity* was introduced. It is defined as:

$$\frac{|f(p, x + \lambda) - f(p, x)|}{f(p, x)} = 1 , \quad (3.28)$$

841 where λ is the homogeneity length. It can be interpreted as the distance at which
 842 relative change of the source Wigner function f becomes large. One can measure

the lengths of homogeneity of a system using femtoscopic radii. This concept can be intuitively explained on a basis of hydrodynamic models. Each source element is emitting particles with a velocity which is a combination of two components: a fluid cell velocity β_f (which is taken from the flow field $u_\mu(x^\mu)$) and thermal velocity β_{th} (which has random direction). These particles can combine into pairs of small relative momenta and become correlated. If two particles are emitted far ($|x_a - x_b| > \lambda$) away from each other, the flow field u_μ in their point of emission might be very different and it will be impossible for them to have sufficiently small relative momenta to be in the region of interference effect. This effect is presented in Fig. 3.4. An increase of a correlation is visible for pairs with low relative momenta [8].

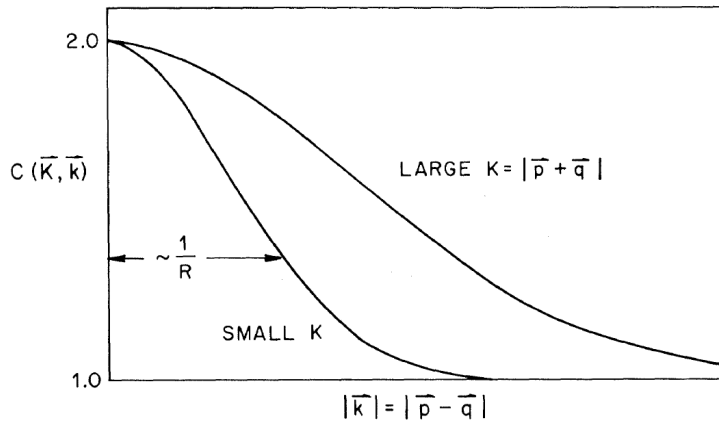


Figure 3.4: Correlation function width dependence on total pair momentum. Pion pairs with a large total momentum have a wider correlation (smaller apparent source) [27].

853

854 3.4.1 Scaling in LCMS

Hydrodynamic calculations performed in LCMS show that femtoscopic radii in outward, sideward, and longitudinal direction show dependence on transverse mass $m_T = \sqrt{k_T^2 + m^2}$, where m is a mass of a particle [28]. Moreover, experimental results show that this scaling is observed for R_{LCMS} radii also. This dependence can be expressed as follows:

$$R_i = \alpha m_T^{-\beta} \quad (3.29)$$

855 where i subscript indicates that this equation applies to R_{out} , R_{side} and R_{long}
 856 radii. The β exponent is approximately equal 0.5. In case of strong transversal
 857 expansion of the emitting source, the decrease of longitudinal interferometry ra-
 858 dius can be more quick than $m_T^{-0.5}$, hence one can expect for longitudinal radii
 859 greater values of $\beta > 0.5$ [28].

860 **3.4.2 Scaling in PRF**

861 In the collisions at the LHC energies, pions are most abundant particles and
 862 their multiplicities are large enough to enable three-dimensional analysis. How-
 863 ever, for heavier particles, such as kaons and protons statistical limitations arise.
 864 Hence it is often possible to only measure one-dimensional direction-averaged
 865 radius R_{inv} for those particles. The R_{inv} is then calculated in the PRF. The trans-
 866 tion from LCMS to PRF is a Lorentz boost in the direction of pair transverse
 867 momentum with velocity $\beta_T = p_T/m_T$. Hence only R_{out} changes:

$$R_{out}^* = \gamma_T R_{out}. \quad (3.30)$$

868 A Lorentz factor $\gamma_T = m_T/m$ depends on the particle type, therefore for the
 869 lighter particles (and for the same m_T) γ_T is much larger, which causes bigger
 870 growth of R_{out} and overall radius. This transformation to PRF breaks the scaling
 871 observed in the LCMS radii.

872 This increase of radius in the outward direction induces overall source
 873 size growth and whatsoever the source distribution function becomes
 874 non-gaussian. In this case the source function is developing long-range tails and
 875 its one-dimensional projection is much narrower than Gaussian distribution.
 876 This deformation is presented in Fig. 3.3. The influence of these effects can be
 877 expressed with an approximate formula:

$$R_{inv} = \sqrt{(R_{out}^2 \sqrt{\gamma_T} + R_{side}^2 + R_{long}^2)/3}. \quad (3.31)$$

878 Because the averaging of the radii is done in quadrature, one would have expec-
 879 ted appearance of γ_T^2 instead of $\sqrt{\gamma_T}$ in this equation. However the Monte-Carlo
 880 procedure shows that this is not the case and the actual growth is smaller than
 881 the naive expectation. Numerical simulations yield that this increase is best de-
 882 scribed with the $\sqrt{\gamma_T}$ in the Eq. 3.31 [29].

Assuming that radii in all directions are equal $R_{out} = R_{side} = R_{long}$, Eq. 3.31
 can be reverted using Eq. 3.15 to express relationship between LCMS and PRF
 overall radii [29]:

$$R_{LCMS} \approx R_{inv} \times [(\sqrt{\gamma_T} + 2)/3]^{-1/2}. \quad (3.32)$$

883 This approximate formula allows to restore power-law behaviour of the scaled
 884 radii not only when the radii are equal, but also when their differences are small
 885 (for explanation see the last part of the Section 3.2.3).

886 This method of recovering scaling in PRF can be used as a tool for the search
 887 of hydrodynamic collectivity between pions, kaons and protons in heavy ion col-
 888 lisions with the measurement of one-dimensional radius in PRF.

889 **Chapter 4**

890 **Results**

891 For the purposes of the femtoscopic analysis in this thesis, the THERMINATOR
892 model was used to generate large number of events for eight different sets of
893 initial conditions corresponding the following centrality ranges: 0-5%, 0-10%, 10-
894 20%, 20-30%, 30-40%, 40-50%, 50-60% and 60-70% for the Pb-Pb collisions at the
895 centre of mass energy $\sqrt{s_{NN}} = 2.76 \text{ TeV}$.

896 **4.1 Identical particles correlations**

897 The correlation functions (three-dimensional and one-dimensional) were cal-
898 culated separately for the following different pairs of identical particles: $\pi-\pi$, $K-$
899 K and $p-p$ for nine k_T bins (in GeV/c): 0.1-0.2, 0.2-0.3, 0.3-0.4, 0.4-0.5, 0.6-0.7,
900 0.7-0.8, 0.8-1.0 and 1.0-1.2. In case of kaons, k_T ranges start from 0.3 and for pro-
901 tons from 0.4 and for both of them the maximum value is 1.0. The k_T ranges for
902 the heavier particles were limited to maintain sufficient multiplicity to perform
903 reliable calculations.

904 **4.1.1 Spherical harmonics components**

905 The three-dimensional correlation function as a function of relative
906 momentum q_{LCMS} was calculated in a form of components of spherical
907 harmonics series accordingly to the Eq. 3.21. In the femtoscopic analysis of
908 identical particles, the most important information is stored in the $\Re C_0^0$, $\Re C_2^0$
909 and $\Re C_2^2$, hence only those components were analyzed. Correlation functions
910 obtained in this procedure were calculated for the different centrality bins for the
911 pairs of pions, kaons and protons. They are presented in the Fig. 4.1, 4.2 and 4.3.

912 Coefficients for pairs of identical bosons (pions and kaons) are shown in the
913 Fig. 4.1 and 4.2. The wave function symmetrization (Bose-Einstein statistics)
914 causes the increase of a correlation in the low relative momenta regime ($q_{LCMS} <$
915 0.06 GeV/c or even $q_{LCMS} < 0.12 \text{ GeV/c}$ for more peripheral collisions). It is
916 clearly visible in the $\Re C_0^0$ component. The $\Re C_0^0$ resembles one-dimensional cor-

relation function and in the sense that it encodes information about the overall source radius. The second coefficient $\Re C_2^0$ differs from zero (is negative), which yields the information about the ratio R_T/R_{long} . The $\Re C_2^2$ stores the information about R_{out}/R_{side} ratio and one can notice that is non-vanishing (is also negative).

The correlation function for a pair of identical fermions is presented in the Fig. 4.3. A wave function for a pair of protons is a composition of singlet (described by Bose-Einstein statistics) and triplet state (described by the Fermi-Dirac statistics - see Section 3.3). An influence of Fermi-Dirac statistics has its effect in the decrease of a correlation down to 0.5 at low relative momentum ($q_{LCMS} < 0.1$ GeV/c or $q_{LCMS} < 0.15$ GeV/c for more peripheral collisions), which can be

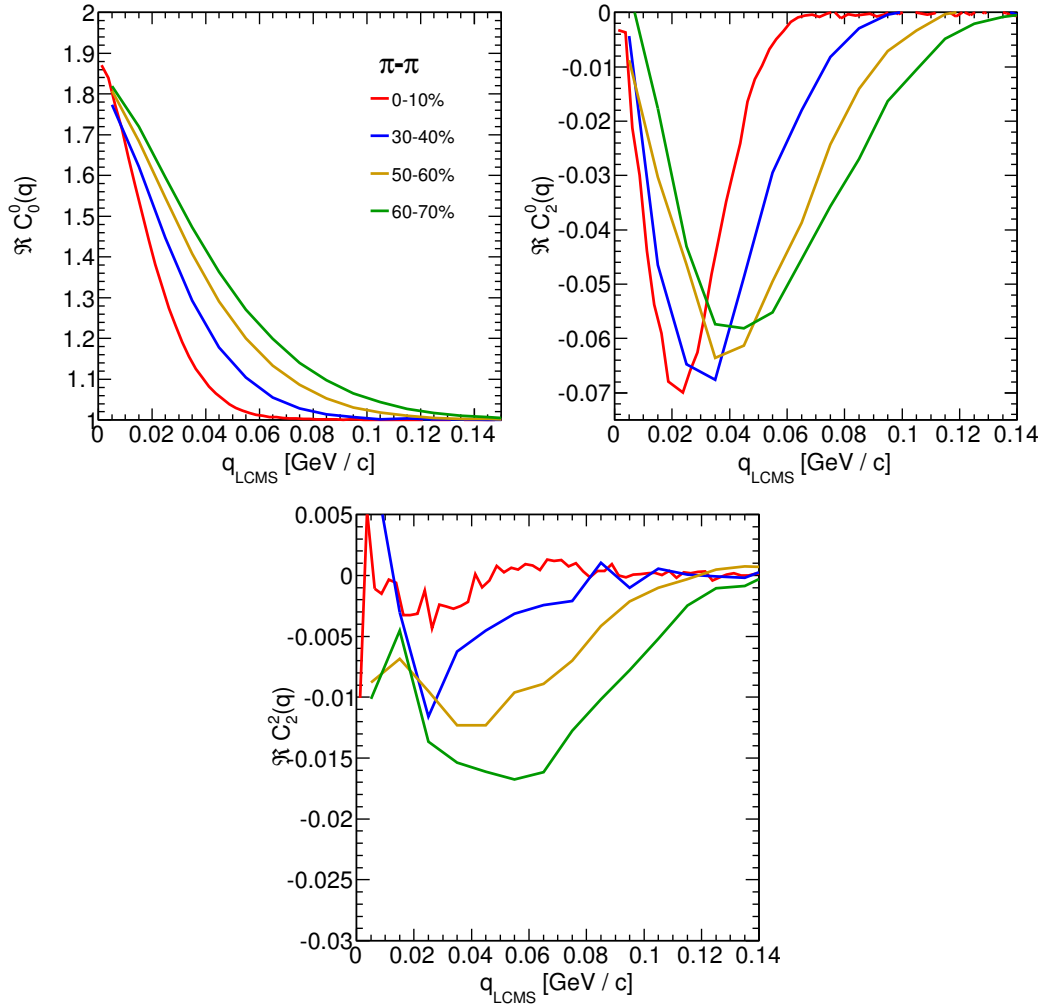


Figure 4.1: Spherical harmonics coefficients of the two-pion correlation function. From the top left: $\Re C_0^0$, $\Re C_2^0$ and $\Re C_2^2$. Only few centrality bins are presented for increased readability.

927 observed in $\Re C_0^0$. The $\Re C_0^0$ and $\Re C_2^2$ coefficients differ from zero and are becoming positive.
 928

929 The common effect of the spherical harmonics form of a correlation function
 930 is the “mirroring” of the shape of the $\Re C_0^0$ coefficient - when correlation function
 931 increases at low q_{LCMS} , the $\Re C_2^0$ and $\Re C_2^2$ are becoming negative and vice
 932 versa. This is quite different behaviour than in the case of correlations of non-
 933 identical particles, where the $\Re C_2^0$ still behaves in the same manner, but $\Re C_2^2$ has
 934 the opposite sign to the $\Re C_2^0$ [25].

935 In all cases, the correlation function gets wider with the peripherality of a

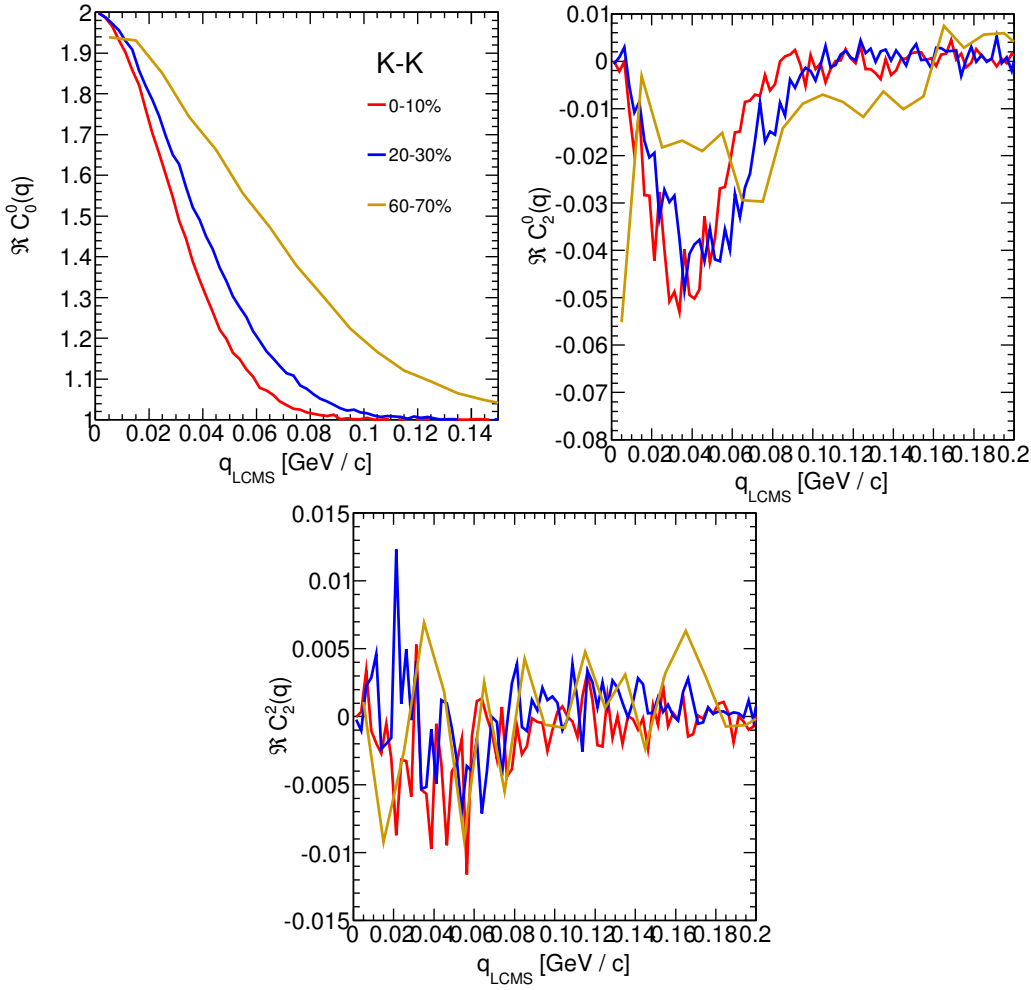


Figure 4.2: Spherical harmonics coefficients of the two-kaon correlation function. From the top left: $\Re C_0^0$, $\Re C_2^0$ and $\Re C_2^2$. Only few centrality bins are presented for increased readability. The $\Re C_2^2$ is noisy, but one can still notice that it differs from zero and is becoming negative.

936 collision i.e. the correlation function for most central collisions (0-10%) is much
 937 narrower than for the most peripheral ones (60-70%). This phenomena in clearly
 938 visible the $\Re C_0^0$ coefficients. Other components are also affected by this effect,
 939 this is especially noticeable in the case of kaons and pions. For the protons, the
 940 results are noisy, hence this effect is not clearly distinguishable.

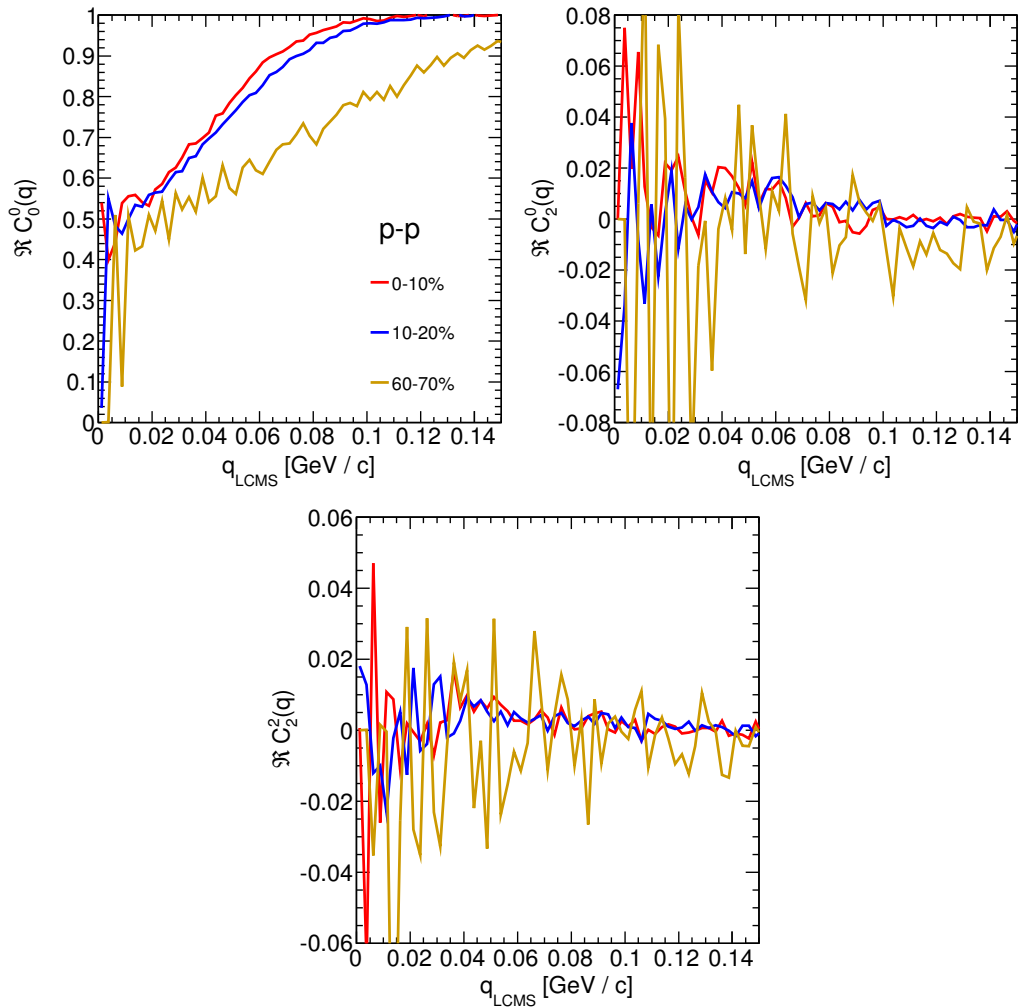


Figure 4.3: Spherical harmonics coefficients of the two-proton correlation function. From the top left: $\Re C_0^0$, $\Re C_2^0$ and $\Re C_2^2$. Only few centrality bins are presented for increased readability. The $\Re C_2^0$ and $\Re C_2^2$ are noisy, but one can still notice, that they differ from zero and are becoming positive.

4.1.2 Centrality dependence of a correlation function

The centrality dependence of a correlation function is especially visible in one-dimensional correlation functions. This effect is presented in the Fig. 4.4 - the correlation functions for pions, kaons and protons are plotted for the same k_T range but different centrality bins. One can notice that the width of a function is smaller in the case of most central collisions. Hence, the femtoscopic radii (proportional to the inverse of width) are increasing with the centrality. An explanation for this growth is that in the most central collisions, a size of a created system is larger than for the peripheral ones.

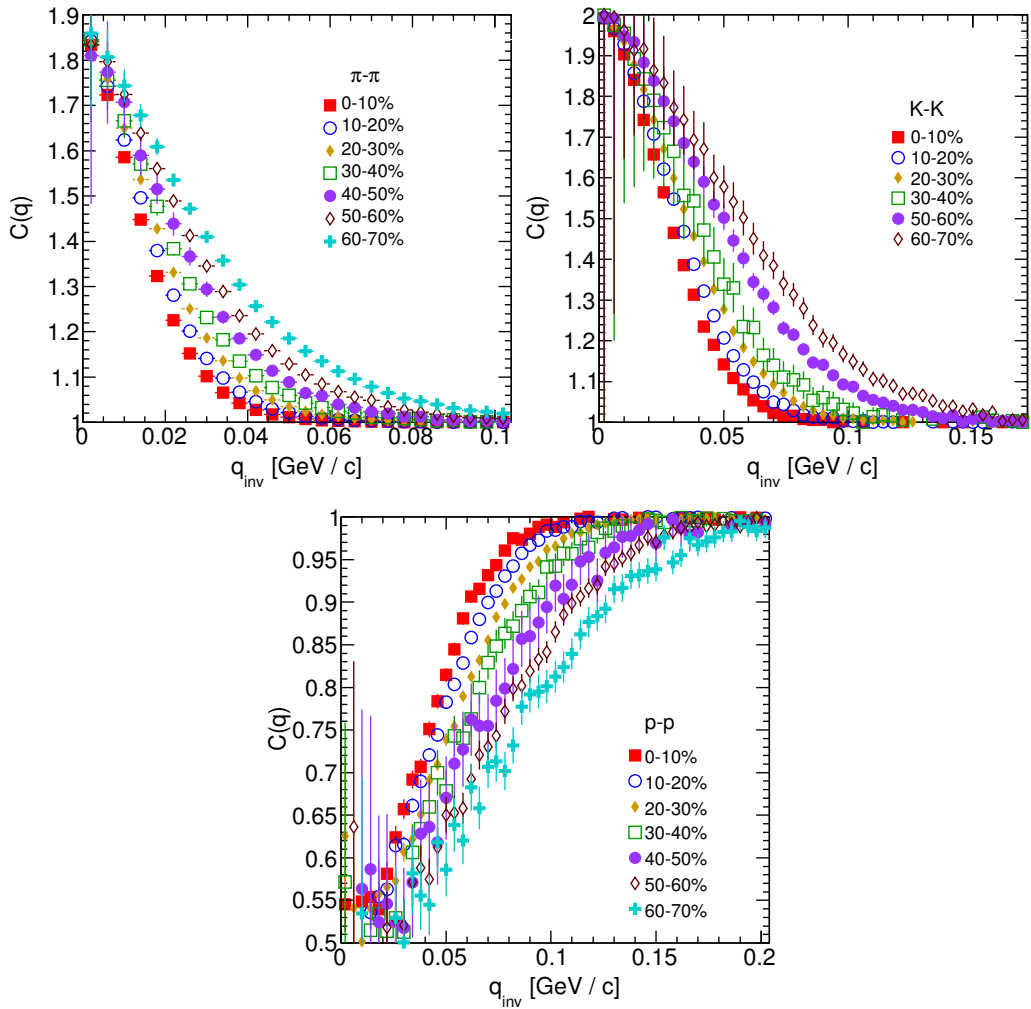


Figure 4.4: One-dimensional correlation function for pions (top left), kaons (top right) and protons (bottom) for different centralities.

4.1.3 k_T dependence of a correlation function

In the Fig. 4.5 there are presented one-dimensional correlation functions for pions, kaons and protons for the same centrality bin, but different k_T ranges. One can observe in all cases of the particle types, appearance of the same trend: with the increase of the total transverse momentum of a pair, the width of a correlation function increases and the femtoscopic radius decreases. The plots in the Fig. 4.5 were zoomed in to show the influence of k_T .

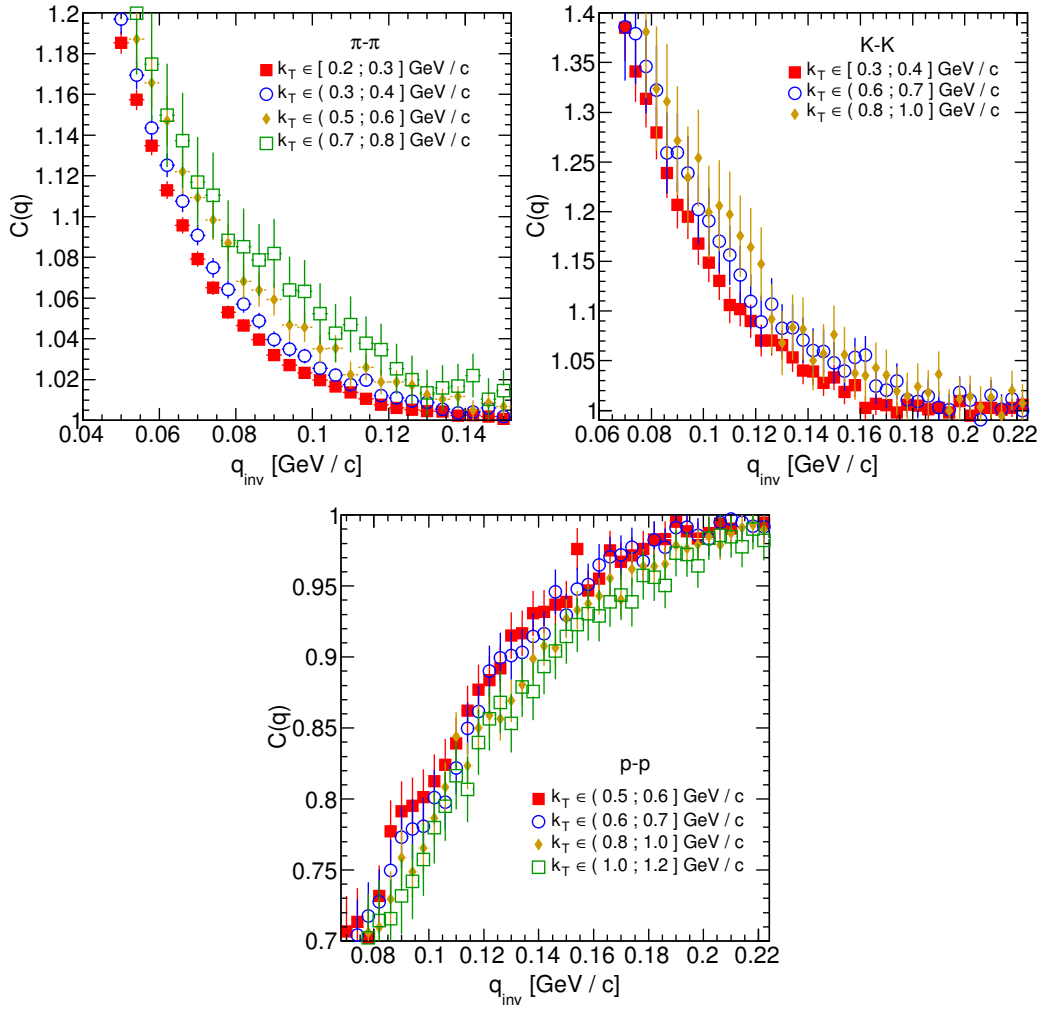


Figure 4.5: One-dimensional correlation functions for pions, kaons and protons, for the same centrality bin and different k_T ranges. The plot was zoomed in to the region which illustrates the k_T dependence in the best way. Only few of the calculated ranges are presented for better readability.

4.2 Results of the fitting procedure

In order to perform a quantitative analysis of a wide range of correlation functions, the theoretical formulas were fitted to the calculated experimental-like data. In this procedure, the femtoscopic radii for the three-dimensional as well as one-dimensional correlation functions were extracted. The main goal of this analysis is a verification of a common transverse mass scaling for different particles types. Obtained radii are plotted as a function of a transverse mass $m_T = \sqrt{k_T^2 + m^2}$. To test the scaling, the following power-law was fitted to the particular radii afterwards:

$$R_x = \alpha m_T^{-\beta}, \quad (4.1)$$

where the α and β are free parameters.

4.2.1 The three-dimensional femtoscopic radii scaling

The femtoscopic radii in the outward, sideward and longitudinal directions for the analysis of two-pion correlation functions in the LCMS are

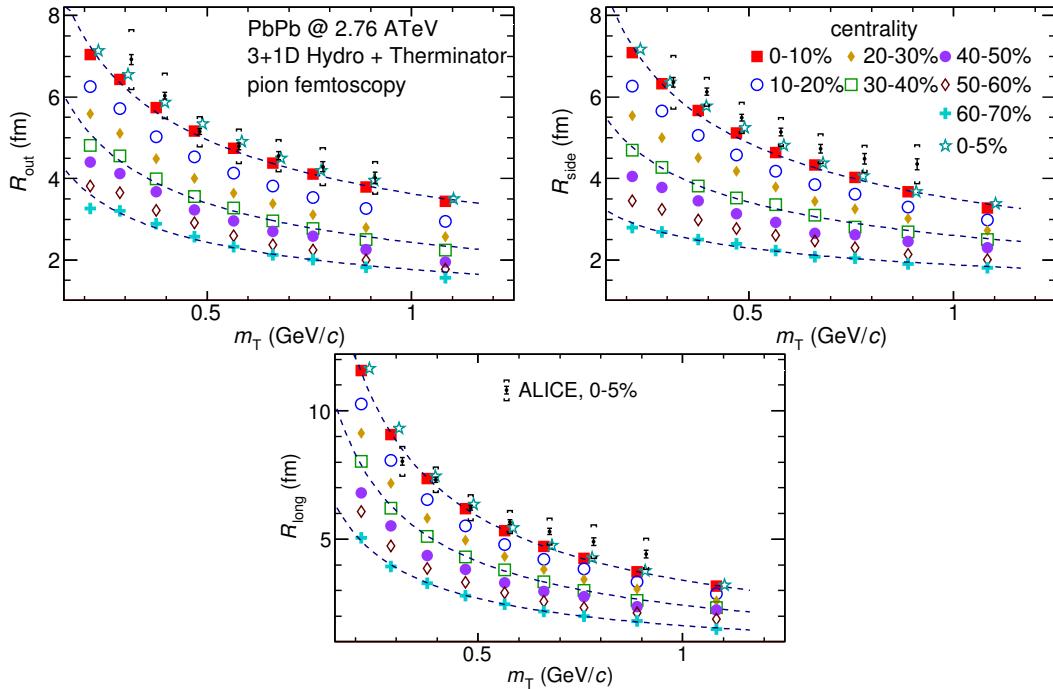


Figure 4.6: Femtoscopic radii in LCMS coming from two-pion correlation functions for all centrality bins as a function of m_T . The dashed lines are power-law fits. The most central collisions (0-5%) are compared to the results from ALICE [30]. The two datasets are shifted to the right for visibility [29].

presented in Fig. 4.6. The dashed lines are fits of the power law to the data. One can notice, that the power law describes data points well with a 5% accuracy. The β fit parameter for the outward direction is in the order of 0.45. For the sideward direction, this parameter has the similar value, but it is lower for the most peripheral collisions. In case of the longitudinal direction, the β has greater value, up to 0.75. In the Fig. 4.6, results for the top 5% central collisions (star-shaped markers) with experimental data from ALICE [30] are also compared. The experimental results are consistent with the ones coming from the model predictions.

The Fig. 4.7 presents femtoscopic radii coming from the kaon calculations. The R_{out} , R_{side} and R_{long} fall also with the power-law within the 5% accuracy. The β parameter was larger in case of kaons: 0.59 in outward direction, 0.54 in the sideward and 0.86 for longitudinal.

The results for two-proton analysis are shown in the Fig. 4.8. The Eq. 4.1 was fitted to the data and tells that the protons also follow the m_T scaling within 5% range. The β parameter values were even bigger for the outward (0.58), sideward (0.61) and longitudinal (1.09) directions than for the other particle types.

The Fig. 4.9 presents results for the pions, kaons and protons together as a function of m_T . Considering differences in the β value for the fits for differ-

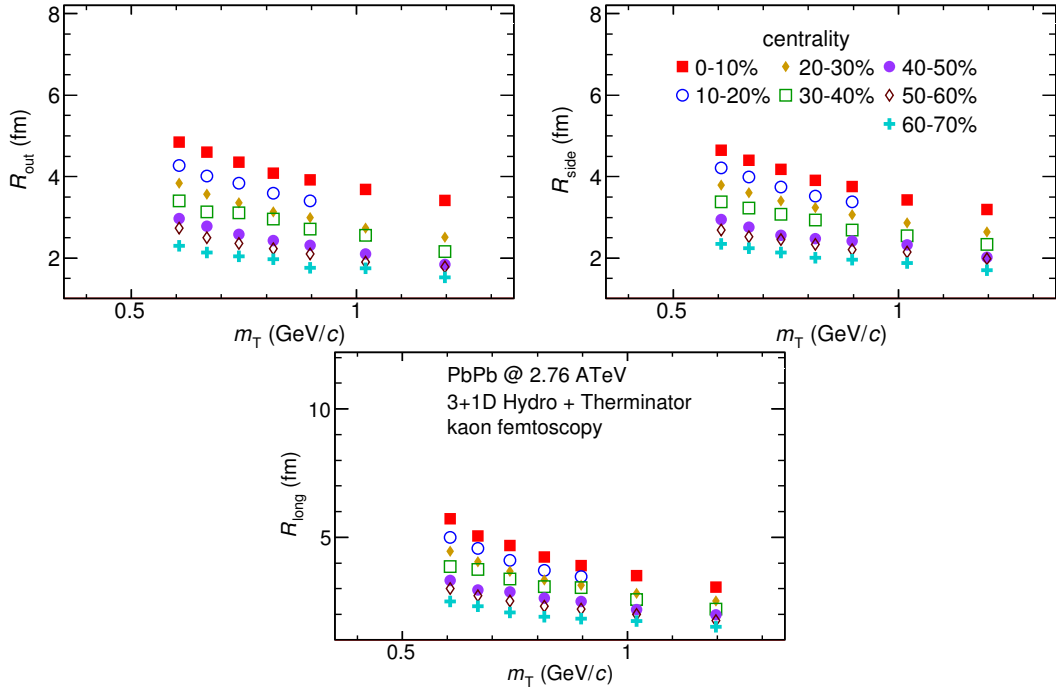


Figure 4.7: Femtoscopic radii extracted from two-kaon correlation functions for different centrality bins as a function of m_T . [29].

ent particles, one can suspect that there is no common scaling between different kinds of particles. However, when all of the results shown on the same plot, they are aligning on the common curve and the scaling is well preserved. The scaling accuracy is 3%, 5% and 4% for the 0-10%, 20-30% and 60-70% for the outward direction. For the sideward radii the scaling is better, with average deviations 2%, 2% and 3% respectively. In case of longitudinal direction the accuracy is 6%, 5% and 3% for the three centralities. The β parameter for the outward direction is close to 0.42 in all cases. For the sideward direction it varies from 0.28 to 0.47 and is bigger for more central collisions. Regarding longitudinal radii, the exponent is bigger than the other two: $\beta \in [0.62; 0.72]$. Considering all results, the plotted radii are following the common power-law scaling within the 5% accuracy for all directions, centralities and particle types.

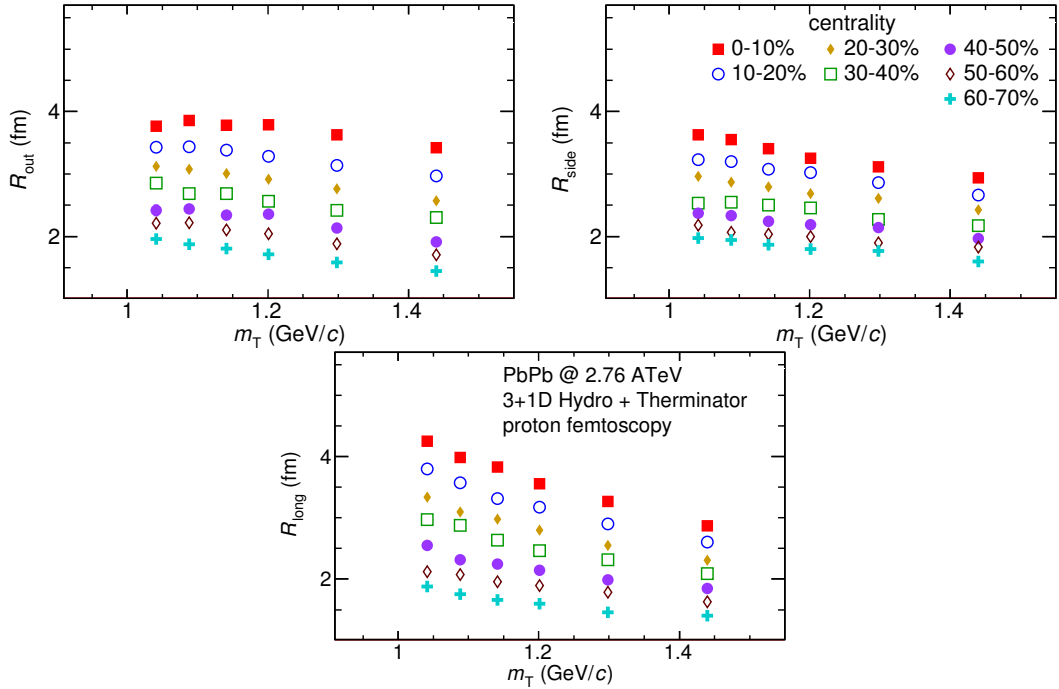


Figure 4.8: Femtoscopic radii extracted from two-proton correlation functions for different centrality bins as a function of m_T . [29].

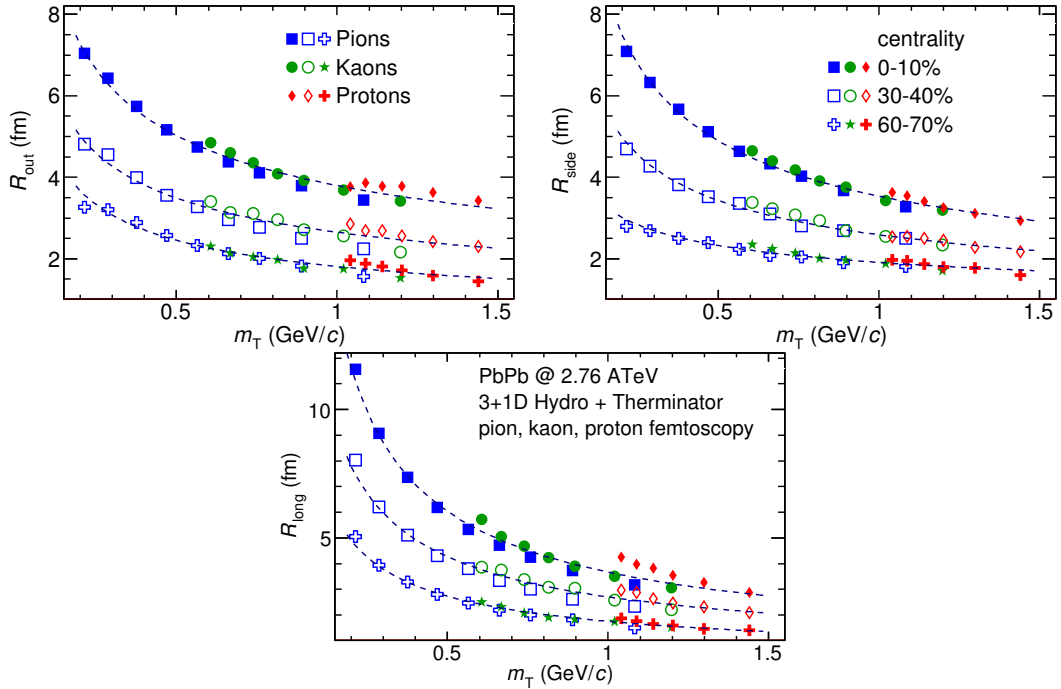


Figure 4.9: The results from the calculations for the pions, kaons and protons in for the three centralities presented on the common plot. One can notice that radii for particular centralities and different particle types follow the common power-law scaling. [29].

4.2.2 Scaling of one-dimensional radii

To the one-dimensional correlation function, the corresponding function in the PRF given by the Eq. 3.18 was fitted. The results from those fits are presented in the upper left plot in the Fig. 4.10. One immediately notices, that there is no common scaling of R_{inv} for different kind of particles. In Fig. 4.9 the radii in the outward direction for the pions, kaons and protons for the same m_T are similar. However, when one performs a transition from the LCMS to the PRF, the R_{out} radius grows:

$$R_{out}^* = \gamma_T R_{out}, \quad (4.2)$$

where $\gamma_T = m_T/m$. For the lighter particles, the γ_T is much larger, hence the bigger growth of the R_{out} and the overall radius. This is visible in the Fig. 4.10 (top left), where the radii in the PRF for the lighter particles are bigger than for the heavier ones in case of the same m_T range.

In the Fig. 4.9 there is visible scaling in the outward, sideward and longitudinal direction. Hence one can expect an appearance of such scaling in a direction-averaged radius calculated in the LCMS. This radius is presented in the Fig. 4.10 (bottom) and indeed the R_{LCMS} exhibits power-law scaling with m_T .

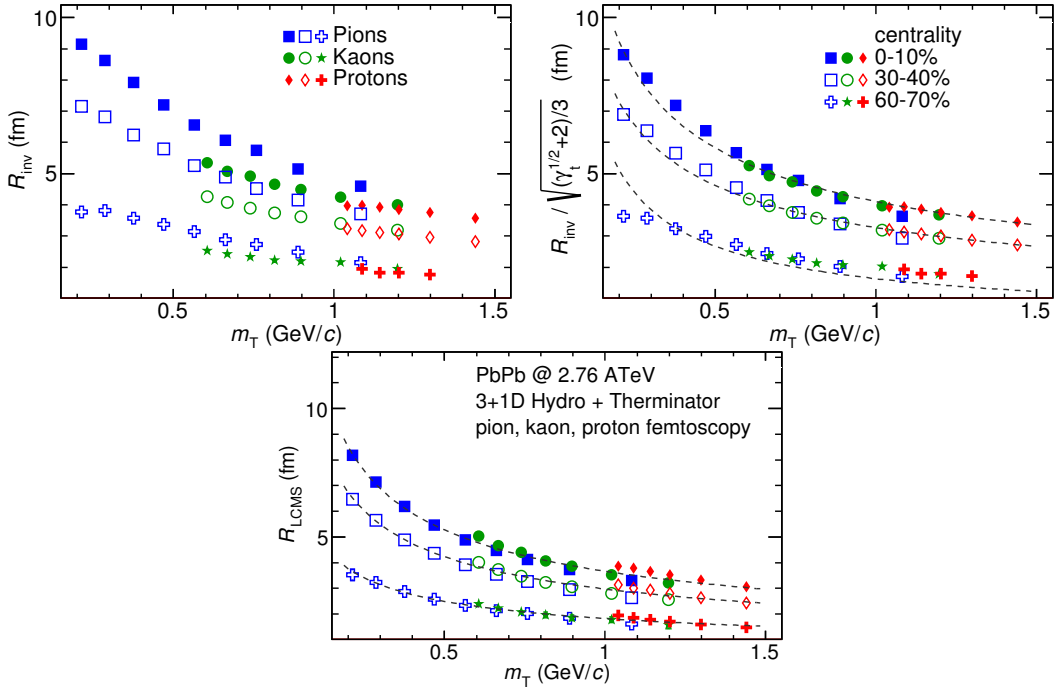


Figure 4.10: Top left: one-dimensional radius for pions, kaons and protons calculated in the PRF. Top right: the R_{inv} scaled by the proposed factor. Bottom: averaged one-dimensional radius in the LCMS for pions, kaons and protons. Only three centrality bins are shown for the better readability [29].

1018 One can try to account the effect of an increase of the radii in the outward direction
 1019 by using the appropriate scaling factor. In Fig. 4.10 (top right), femtoscopic
 1020 radii in the LCMS are divided by the proposed scaling factor:

$$f = \sqrt{(\sqrt{\gamma_T} + 2)/3} . \quad (4.3)$$

1021 The radii for pions, kaons and protons in the PRF after the division by f are
 1022 following the power-law with the accuracy of 10%.

1023 4.3 Discussion of the results

1024 The femtoscopic radii obtained from the three-dimensional correlation func-
 1025 tion fitting exhibit the m_T dependence described by the power law (Eq. 4.1). This
 1026 scaling is preserved quite well with accuracy <10%. Observation of such scaling
 1027 in a femtoscopic radii is a strong signal of the appearance of a collective beha-
 1028 viour of a particle-emitting source created in the collision. The data used in the
 1029 analysis was coming from the hydrodynamic model, hence one can indeed ex-
 1030 pect the appearance of this scaling. However, the results for pion femtoscopy
 1031 from the ALICE at LHC are consistent with the data from analysis performed in
 1032 this thesis (Fig. 4.6). This is a confirmation of an applicability of hydrodynamic
 1033 models in a description of an evolution of a quark-gluon plasma.

1034 The β parameter calculated in the fitting of the power-law to the femtoscopic
 1035 radii is of the order of 0.5 in case of the radii in the transverse plane. This value is
 1036 consistent with the hydrodynamic predictions. In case of longitudinal radii, the
 1037 exponent is bigger (greater than 0.7), which is an indication of a strong transversal
 1038 expansion in the system [28].

1039 A scaling described above is visible in the LCMS, however due to limited
 1040 statistics, analysis in this reference frame is not always possible. In such case
 1041 one performs calculations in the PRF. The m_T scaling in the PRF is not observed
 1042 - this has a trivial kinematic origin. A transition from the PRF to LCMS causes
 1043 growth of the radius in the outward direction and the common power-law scal-
 1044 ing for different particles breaks due to differences in the $\gamma_T(m_T)$ for different
 1045 particle types. However one can try to deal with the radius growth and restore
 1046 the scaling by dividing the radii R_{inv} by an approximate factor $\sqrt{(\sqrt{\gamma_T} + 2)/3}$.
 1047 The scaled R_{inv} are following the power-law and could be used as a verification
 1048 of hydrodynamic behaviour in the investigated particle source.

1049 The hadronic evolution and freeze-out in the THERMINATOR is followed
 1050 by the resonance propagation and decay phase. A good accuracy of a scaling
 1051 with the power-law indicated that the inclusion of the resonances does not
 1052 break the m_T scaling. However, recent calculations including also hadron
 1053 rescattering phase indicate that the scaling between pions and kaons is broken
 1054 at the LHC [31].

1055 Conclusions

1056 This thesis presents the results of the two-particle femtoscopy of different
1057 particle kinds produced in Pb-Pb collisions at the centre of mass energy
1058 $\sqrt{s_{NN}} = 2.76$ TeV. The analysed data was generated by the THERMINATOR
1059 model using the (3+1)-dimensional hydrodynamic model.

1060 The momentum correlations were studied for three different types of particle
1061 pairs: pions, kaons and protons. The data was analyzed for eight different sets
1062 of initial conditions corresponding the following centrality ranges: 0-5%, 0-10%,
1063 10-20%, 20-30%, 30-40%, 40-50%, 50-60% and 60-70%. The correlation functions
1064 were calculated for the nine k_T bins from 0.1 GeV/c to 1.2 GeV/c. The cal-
1065 culations were performed using spherical harmonics decomposition of a three-
1066 dimensional correlation function. Using this approach, one can obtain full three-
1067 dimensional information about the source size using only the three coefficients:
1068 $\Re C_0^0$, $\Re C_2^0$ and $\Re C_2^2$. To perform further quantitative analysis, the femtoscopic
1069 radii were extracted through fitting.

1070 The calculated correlation functions show expected increase of a correlation
1071 at low relative momenta in case of identical bosons (pions and kaons) and the
1072 decrease for the identical fermions (protons) respectively. This effect is especially
1073 visible in the first spherical harmonic coefficient $\Re C_0^0$. The other two components
1074 $\Re C_2^0$ and $\Re C_2^2$ are non-vanishing and are providing information about the ratios
1075 of radii in the outward, sideward and longitudinal directions.

1076 An increase of width of a correlation function with the peripherality of a colli-
1077 sion and the k_T is observed for pions, kaons and protons. This increase of femto-
1078scopic radii (proportional to the inverse of width) with the k_T is related with the
1079 m_T scaling predicted by the hydrodynamic calculations.

1080 Hydrodynamic equations are predicting appearance of femtoscopic radii
1081 common scaling for different kinds of particles with the $m_T^{-0.5}$ in the LCMS.
1082 In the results in this work, a common scaling for different particle types is
1083 observed in the LCMS in the outward, sideward and longitudinal direction. The
1084 direction-averaged radius R_{LCMS} also shows this power-law behaviour. The
1085 fitting of a power law $\alpha m_T^{-\beta}$ to the femtoscopic radii yielded the information,
1086 that the β exponent for the outward and sideward direction is in order of 0.5,
1087 which is consistent with the hydrodynamic predictions. For the longitudinal
1088 direction, the β is bigger (>0.7) than in the other directions which is an indication
1089 of a strong transverse flow. Femtoscopic radii in LCMS are following the

1090 power-law scaling with the accuracy <5% for pions and kaons, and <10% in case
1091 of protons.

1092 In case of the one-dimensional radii R_{inv} calculated in the PRF, no common
1093 scaling is observed. This is a consequence of a transition from the LCMS to the
1094 PRF, which causes the growth of radius in the outward direction and breaks the
1095 scaling for different particles. However, one can try to correct the influence of
1096 the R_{out} growth with an approximate factor $\sqrt{(\sqrt{\gamma_T} + 2)/3}$. After the division
1097 of the R_{inv} by the proposed factor, the scaling is restored with an accuracy <10%.
1098 In this way, the experimentally simpler measure of the one-dimensional radii can
1099 be used as a probe for the hydrodynamic collectivity.

1100 The THERMINATOR model includes hydrodynamic expansion, statistical had-
1101 ronization, resonance propagation and decay afterwards. The m_T scaling is pre-
1102 dicted from the pure hydrodynamic calculations. However, this study shows,
1103 that influence of the resonances on this scaling is less than 10%.

1104 **Appendix A**

1105 **Scripts for correlation function
1106 calculations**

1107 **A.1 Events generation**

1108 In order to perform analysis with sufficient statistics, a large amount of gen-
1109 erated events was required. To handle this task of generation large amount of
1110 data, a computer cluster at Faculty of Physics at Warsaw University of Techno-
1111 logy was used. This cluster consists of 20 nodes with the following hardware
1112 configuration: Intel® Core™ 2 Quad CPU Q6600 @ 2.40GHz, 8GB RAM with Sci-
1113 entific Linux 5.8. The communication between nodes is realized by the TORQUE
1114 Resource Manager [32]. To control process of launching multiple event gener-
1115 ators and collecting the data, the following scripts were written using Bash script-
1116 ing language:

1117 **skynet.sh** This is a script in a form of a batch job for TORQUE. It simply
1118 launches multiple THERMINATOR processes in the same working directory
1119 with the separate output directory for each job. This solution has two
1120 advantages: saves space and computation time. A single freeze-out
1121 hypersurface file has size about 230 MB and when running 20 instances
1122 of generator this approach allows to avoid time- and space-consuming
1123 copying of the whole THERMINATOR directory before running the
1124 application. The second advantage is a sharing of files containing
1125 information about particles' multiplicities and maximum integrands
1126 between generator processes (more detailed description is in Section 2.3).
1127 One can simply execute this batch job using the following command (an
1128 example usage):

1129 `qsub -q long -t 0-19 skynet.sh -v dir=th_5.7,events=6000`
1130 It adds 20 event generators (with task ids from 0 to 19) to the queue, sets
1131 the THERMINATOR directory as `th_5.7` and sets a number of simulated
1132 events to 6000 for each process. One has to execute this command in the
1133 directory one level higher than `th_5.7` directory.

1134 **merge_events.sh** After the generation process, one has to merge calculated
 1135 events into one directory. This task requires renaming of a large number of
 1136 THERMINATOR event files. Each event generator job produces files named
 1137 with a certain pattern, starting from event000.root with increasing number.
 1138 In order to move the event files and preserve continuity in the numbering,
 1139 a simple script was written. An example of usage:

1140 `find /data/source -iname "event*.root" -type f \`
 1141 `| merge_events.sh`

1142 This command will find all the event files in the directory /data/source,
 1143 move and rename those files accordingly to the enumeration of events in
 1144 the current working directory.

1145 Sources of these two scripts are available on-line at <https://github.com/>
 1146 `carbolymer/msc/tree/master/alix`.

1147 **A.2 Calculations of experimental-like correlation
 1148 functions**

1149 TODO

₁₁₅₀ **Appendix B**

₁₁₅₁ **Macros for fitting**

1152 Appendix C

1153 Plotting scripts

Bibliography

- [1] Standard Model of Elementary Particles - Wikipedia, the free encyclopedia
http://en.wikipedia.org/wiki/standard_model.
- [2] R. Aaij et al. (LHCb Collaboration). Observation of the resonant character of the $z(4430)^-$ state. *Phys. Rev. Lett.*, 112:222002, Jun 2014.
- [3] Donald H. Perkins. *Introduction to High Energy Physics*. Cambridge University Press, fourth edition, 2000. Cambridge Books Online.
- [4] G. Odyniec. *Phase Diagram of Quantum Chromo-Dynamics* - course at Faculty of Physics, Warsaw University of Technology, Jun 2012.
- [5] J. Beringer et al. (Particle Data Group). The Review of Particle Physics. *Phys. Rev.*, D86:010001, 2012.
- [6] Z. Fodor and S.D. Katz. The Phase diagram of quantum chromodynamics. 2009.
- [7] F. Karsch. Lattice results on QCD thermodynamics. *Nuclear Physics A*, 698(1-4):199 – 208, 2002.
- [8] Adam Kisiel. *Studies of non-identical meson-meson correlations at low relative velocities in relativistic heavy-ion collisions registered in the STAR experiment*. PhD thesis, Warsaw University of Technology, Aug 2004.
- [9] J. Bartke. *Relativistic Heavy Ion Physics*. World Scientific Pub., 2009.
- [10] W. Florkowski. *Phenomenology of Ultra-Relativistic Heavy-Ion Collisions*. World Scientific, 2010.
- [11] Science Grid This Week, October 25, 2006 - Probing the Perfect Liquid with the STAR Grid
http://www.interactions.org/sgtw/2006/1025/star_grid_more.html.
- [12] K. Grebieszkow. Fizyka zderzeń ciężkich jonów,
<http://www.if.pw.edu.pl/~kperl/hip/hip.html>.
- [13] Ulrich W. Heinz. From SPS to RHIC: Maurice and the CERN heavy-ion programme. *Phys. Scripta*, 78:028005, 2008.

- 1182 [14] J. Adams et al. Identified particle distributions in pp and Au+Au collisions
1183 at $s(\text{NN})^{**}(1/2) = 200 \text{ GeV}$. *Phys.Rev.Lett.*, 92:112301, 2004.
- 1184 [15] G. David, R. Rapp, and Z. Xu. Electromagnetic Probes at RHIC-II. *Phys.Rept.*,
1185 462:176–217, 2008.
- 1186 [16] A. Marin et al. Dilepton measurements with CERES. *PoS*, CPOD07:034,
1187 2007.
- 1188 [17] J. Adams et al. Experimental and theoretical challenges in the search for the
1189 quark gluon plasma: The STAR Collaboration’s critical assessment of the
1190 evidence from RHIC collisions. *Nucl.Phys.*, A757:102–183, 2005.
- 1191 [18] Adam Kisiel, Tomasz Taluc, Wojciech Broniowski, and Wojciech
1192 Florkowski. THERMINATOR: THERMal heavy-IoN generATOR. *Comput.Phys.Commun.*, 174:669–687, 2006.
- 1194 [19] Mikolaj Chojnacki, Adam Kisiel, Wojciech Florkowski, and Wojciech Bro-
1195 niowski. THERMINATOR 2: THERMal heavy IoN generATOR 2. *Comput.Phys.Commun.*, 183:746–773, 2012.
- 1197 [20] I. et al (BRAHMS Collaboration) Bearden. Charged meson rapidity distri-
1198 butions in central Au + Au collisions at $\sqrt{s_{\text{NN}}} = 200 \text{ GeV}$. *Phys. Rev. Lett.*,
1199 94:162301, Apr 2005.
- 1200 [21] W. Israel and J.M. Stewart. Transient relativistic thermodynamics and kin-
1201 etic theory. *Annals of Physics*, 118(2):341 – 372, 1979.
- 1202 [22] Piotr Bożek. Flow and interferometry in (3 + 1)-dimensional viscous hydro-
1203 dynamics. *Phys. Rev. C*, 85:034901, Mar 2012.
- 1204 [23] K. Kovtun, P. D. T. Son, and A. O. Starinets. Viscosity in strongly interacting
1205 quantum field theories from black hole physics. *Phys. Rev. Lett.*, 94:111601,
1206 Mar 2005.
- 1207 [24] Fred Cooper and Graham Frye. Single-particle distribution in the hydro-
1208 dynamic and statistical thermodynamic models of multiparticle production.
1209 *Phys. Rev. D*, 10:186–189, Jul 1974.
- 1210 [25] Adam Kisiel. Nonidentical-particle femtoscopy at $\sqrt{s_{\text{NN}}} = 200 \text{ GeV}$ in hy-
1211 drodynamics with statistical hadronization. *Phys. Rev. C*, 81:064906, Jun
1212 2010.
- 1213 [26] Adam Kisiel and David A. Brown. Efficient and robust calculation of femto-
1214 scopic correlation functions in spherical harmonics directly from the raw
1215 pairs measured in heavy-ion collisions. *Phys.Rev.*, C80:064911, 2009.
- 1216 [27] S. Pratt. Pion Interferometry for Exploding Sources. *Phys.Rev.Lett.*, 53:1219–
1217 1221, 1984.

- 1218 [28] S.V. Akkelin and Yu.M. Sinyukov. The HBT-interferometry of expanding
1219 inhomogeneous sources. *Z.Phys.*, C72:501–507, 1996.
- 1220 [29] A. Kisiel, M. Galazyn, and P. Bozek. Pion, kaon, and proton femtoscopy in
1221 Pb–Pb collisions at $\sqrt{s_{NN}}=2.76$ TeV modeled in 3+1D hydrodynamics. 2014.
- 1222 [30] K. Aamodt et al. Two-pion Bose-Einstein correlations in central Pb-Pb colli-
1223 sions at $\sqrt{s_{NN}} = 2.76$ TeV. *Phys.Lett.*, B696:328–337, 2011.
- 1224 [31] V.M. Shapoval, P. Braun-Munzinger, Iu.A. Karpenko, and Yu.M. Sinyukov.
1225 Femtoscopy correlations of kaons in $Pb + Pb$ collisions at LHC within hy-
1226 drokinetic model. 2014.
- 1227 [32] TORQUE Resource Manager - An open source resource manager
1228 providing control over batch jobs and distributed compute nodes
1229 <http://www.adaptivecomputing.com/products/open-source/torque/>.

List of Figures

1.1	The Standard Model of elementary particles [1].	3
1.2	A string breaking and a creation of a new quark-anti-quark pair [4].	5
1.3	The coupling parameter α_s dependence on four-momentum transfer Q^2 [5].	6
1.4	The QCD potential for a quark-antiquark pair as a function of distance for different temperatures. A value of a potential decreases with the temperature [4].	7
1.5	A number of degrees of freedom as a function of a temperature [7].	7
1.6	Phase diagram coming from the Lattice QCD calculations [8].	8
1.7	Left: stages of a heavy ion collision simulated in the UrQMD model. Right: schematic view of a heavy ion collision evolution [8].	9
1.8	Overlapping region which is created in heavy ion collisions has an almond shape. Visible x-z plane is a <i>reaction plane</i> . The x-y plane is a <i>transverse plane</i> . The z is a direction of the beam [11].	11
1.9	Cross-section of a heavy ion collision in a transverse plane. The b parameter is an <i>impact parameter</i> - a distance between centers of nuclei during a collision. An impact parameter is related with the centrality of a collision and a volume of the quark-gluon plasma [12].	12
1.10	<i>Lower:</i> The elliptic flow v_2 follows the hydrodynamical predictions for an ideal fluid perfectly. Note that > 99% of all final hadrons have $p_T < 1.5 \text{ GeV}/c$. <i>Upper left:</i> The v_2 plotted versus transverse kinetic energy $KE_T = m_T - m_0 = \sqrt{p_T^2 + m_0^2} - m_0$. The v_2 follows different universal curves for mesons and baryons. <i>Upper right:</i> When scaled by the number of valence quarks, the v_2 follows the same universal curve for all hadrons and for all values of scaled transverse kinetic energy [13].	13
1.11	Invariant yield of particles versus transverse mass $m_T = \sqrt{p_T^2 + m_0^2}$ for π^\pm , K^\pm , p and \bar{p} at mid-rapidity for p+p collisions (bottom) and Au+Au events from 70-80% (second bottom) to 0-5% (top) centrality [14].	14

1261	1.12 Thermal photons spectra for the central Au+Au collisions at			
1262	$\sqrt{s_{NN}} = 200$ GeV computed within different hydrodynamical			
1263	models compared with the pQCD calculations (solid line) and			
1264	experimental data from PHENIX (black dots) [15].	15		
1265	1.13 Left: Invariant mass spectrum of e^+e^- pairs in Pb+Au collisions			
1266	at 158A GeV compared to the sum coming from the hadron decays			
1267	predictions. Right: The expectations coming from model calcula-			
1268	tions assuming a dropping of the ρ mass (blue) or a spread of the			
1269	ρ width in the medium (red) [16].	16		
1270	1.14 Azimuthal angle difference $\Delta\phi$ distributions for different colliding			
1271	systems at $\sqrt{s_{NN}} = 200$ GeV. Transverse momentum cut: $p_T > 2$			
1272	GeV. For the Au+Au collisions the away-side jet is missing [17]. . .	17		
1273	2.1 The cascade decay in the single freeze-out model. An unstable res-			
1274	onance x_N is formed at the freeze-out hypersurface and travels for			
1275	the time τ_N depending on its lifetime and decays. If the products			
1276	are also resonances (x_{N-1}, x_2) they decay further until the stable			
1277	particles are formed (x_1) [18].	24		
1278	3.1 Bertsch-Pratt direction naming convention used in heavy ion col-			
1279	lision.	26		
1280	3.2 The pair wave function is a superposition of all possible states. In			
1281	case of particle interferometry it includes two cases: particles with			
1282	momenta p_1, p_2 registered by detectors A, B and p_1, p_2 registered			
1283	by B, A respectively.	27		
1284	3.3 An averaged three-dimensional Gaussian source function with dif-			
1285	ferent widths was averaged into one-dimensional function. To il-			
1286	lustrate deformations, one-dimensional Gaussian distribution was			
1287	fitted.	30		
1288	3.4 Correlation function width dependence on total pair momentum.			
1289	Pion pairs with a large total momentum have a wider correlation			
1290	(smaller apparent source) [27].	34		
1291	4.1 Spherical harmonics coefficients of the two-pion correlation func-			
1292	tion. From the top left: $\Re C_0^0$, $\Re C_2^0$ and $\Re C_2^2$. Only few centrality			
1293	bins are presented for increased readability.	37		
1294	4.2 Spherical harmonics coefficients of the two-kaon correlation func-			
1295	tion. From the top left: $\Re C_0^0$, $\Re C_2^0$ and $\Re C_2^2$. Only few centrality			
1296	bins are presented for increased readability. The $\Re C_2^2$ is noisy, but			
1297	one can still notice that it differs from zero and is becoming negative.	38		

1298	4.3	Spherical harmonics coefficients of the two-proton correlation function. From the top left: $\Re C_0^0$, $\Re C_2^0$ and $\Re C_2^2$. Only few centrality bins are presented for increased readability. The $\Re C_2^0$ and $\Re C_2^2$ are noisy, but one can still notice, that they differ from zero and are becoming positive.	39
1299			
1300			
1301			
1302			
1303	4.4	One-dimensional correlation function for pions (top left), kaons (top right) and protons (bottom) for different centralities.	40
1304			
1305	4.5	One-dimensional correlation functions for pions, kaons and protons, for the same centrality bin and different k_T ranges. The plot was zoomed in to the region which illustrates the k_T dependence in the best way. Only few of the calculated ranges are presented for better readability.	41
1306			
1307			
1308			
1309			
1310	4.6	Femtoscopic radii in LCMS coming from two-pion correlation functions for all centrality bins as a function of m_T . The dashed lines are power-law fits. The most central collisions (0-5%) are compared to the results from ALICE [30]. The two datasets are shifted to the right for visibility [29].	42
1311			
1312			
1313			
1314			
1315	4.7	Femtoscopic radii extracted from two-kaon correlation functions for different centrality bins as a function of m_T . [29].	43
1316			
1317	4.8	Femtoscopic radii extracted from two-proton correlation functions for different centrality bins as a function of m_T . [29].	44
1318			
1319	4.9	The results from the calculations for the pions, kaons and protons in for the three centralities presented on the common plot. One can notice that radii for particular centralities and different particle types follow the common power-law scaling. [29].	45
1320			
1321			
1322			
1323	4.10	Top left: one-dimensional radius for pions, kaons and protons calculated in the PRF. Top right: the R_{inv} scaled by the proposed factor. Bottom: averaged one-dimensional radius in the LCMS for pions, kaons and protons. Only three centrality bins are shown for the better readability [29].	46
1324			
1325			
1326			
1327			